

Specific Heat and the gap structure of a Nematic Superconductor, application to FeSe

Kazi Ranjibul Islam^{1*}, Jakob Böker^{2*}, Ilya M. Eremin², and Andrey V. Chubukov¹
¹*School of Physics and Astronomy and William I. Fine Theoretical Physics Institute,
 University of Minnesota, Minneapolis, MN 55455, USA and*
²*Institut für Theoretische Physik III, Ruhr-Universität Bochum, 44801 Bochum, Germany*
 (Dated: June 28, 2021)

We report the results of our in-depth analysis of spectroscopic and thermodynamic properties of a multi-orbital metal, like FeSe, which first develops a nematic order and then undergoes a transition into a superconducting state, which co-exists with nematicity. We analyze the angular dependence of the gap function and specific heat $C_V(T)$ of such nematic superconductor. We specifically address three issues: (i) angular dependence of the gap in light of the competition between nematicity-induced s - d mixture and orbital transmutation of low-energy excitations in the nematic state, (ii) the effect of nematicity on the magnitude of the jump of the specific heat $C_V(T)$ at T_c and the temperature dependence of $C_V(T)$ below T_c , and (iii) a potential transition at $T_{c1} < T_c$ from an $s + d$ state to an $s + e^{iv}d$ state that breaks time-reversal symmetry. We consider two scenarios for a nematic order: scenario A, in which this order develops between d_{xz} and d_{yz} orbitals on hole and electron pockets and scenario B, in which there is an additional component of the nematic order for d_{xy} fermions on the two electron pockets.

I. INTRODUCTION.

Iron-based unconventional superconductors demonstrate remarkable properties, which include multi-orbital low-energy electronic states and ubiquity of the nematic phase. A particularly interesting situation occurs when superconductivity is preceded by the development of a nematic order that breaks C_4 lattice rotational symmetry down to C_2 . The most prominent example of this so-called nematic superconductor is FeSe, in which a nematic order develops at $T_n \sim 90K$ at ambient pressure, while superconductivity develops at a much lower $T_c \sim 9K$, out of a nematic state [1,2]. Nematic superconductivity has been observed also in other Fe-based materials, but there the difference between T_n and T_c is much smaller [3]. It has been also argued that in some cases a nematic order does not exist in the normal state but is induced by superconductivity. A candidate for such behavior in the Fe-family is LiFeAs [4]; the same behavior has been reported in twisted bilayer graphene [5] and in doped topological insulator $R_x\text{Bi}_2\text{Se}_3$ ($R=\text{Cu, Nb, and Sr}$) [6–9]. In this work, we focus on the theoretical analysis of the spectroscopic and the thermodynamic properties of such a nematic superconductor using the case of FeSe, where T_n is substantially larger than T_c .

The electronic structure of FeSe in the tetragonal phase consists of two hole pockets, centered around the Γ point (the inner one and the outer one), and electron pockets, centered around the X and the Y points of the Brillouine Zone, respectively (Fig. 1(a)). Here, we use the notation of the 1-Fe unit cell. The hole pockets and the corresponding bands are composed of fermions from d_{xz} and d_{yz} orbitals, the X -pocket/band is a mixture of d_{yz} and d_{xy} orbitals, and the Y -pocket/band is a mixture of d_{xz} and d_{xy} orbitals. ARPES studies revealed that in FeSe the inner hole pocket is quite small in the tetragonal phase and disappears in the presence of a

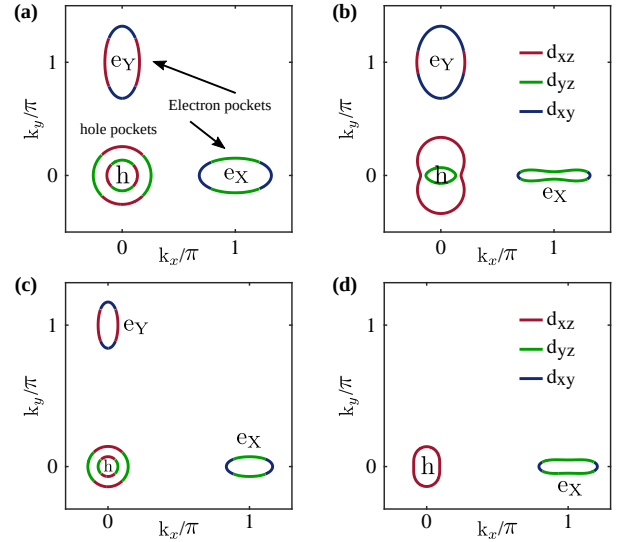


FIG. 1. Fermi surface topology in 1-Fe unit cell of FeSe in the tetragonal phase (a,c) and the orthorhombic (nematic) phase (b,d). The Fermi surface evolution in (b) results from sign-changing nematic order involving d_{xz} and d_{yz} orbitals, in (d) it additionally involves sizable non-local d_{xy} nematic order. We refer to panels (b) and (d) as "scenario A" and "scenario B", respectively. The color code follows the major orbital content. Fitting parameters for (a,b) are taken from Refs. [3,10] and for (c,d) from Ref. [11].

nematic order, when the corresponding band sinks below the Fermi level [12] (Fig. 1(b)). The inner hole band then does not affect system behavior at low energies and we neglect it in our analysis. For the outer hole pocket, the orbital content in the tetragonal phase is predominantly d_{xz} along the k_y -direction and d_{yz} along the k_x -direction.

We consider two scenarios for the nematic order, Φ . In the first (scenario A) we assume that Φ splits the occu-

pations of d_{xz} and d_{yz} orbitals:

$$\Phi_{xz/yz} = \langle d_{xz}^\dagger d_{xz} - d_{yz}^\dagger d_{yz} \rangle \quad (1)$$

Furthermore, we follow earlier theoretical and experimental studies [13–17], which showed that such Φ changes sign between hole and electron pockets. We label Φ on the outer hole pocket as Φ_h and the one on the Y and the X electron pockets as Φ_e ($\text{sgn } \Phi_e = -\text{sgn } \Phi_h$). In the second scenario (scenario B), we assume that in addition to $\Phi_{h,e}$, nematicity gives rise to a substantial difference between occupations of d_{xy} fermions on the Y and the X pockets [11, 13, 18]. The corresponding nematic order parameter is then given by

$$\Phi_{xy} = \langle d_{xy,Y}^\dagger d_{xy,Y} - d_{xy,X}^\dagger d_{xy,X} \rangle. \quad (2)$$

Scenario B was recently advanced in Ref. [11] as a way to explain the thermal evolution of the band structure across the tetragonal to orthorhombic transition as well as the fact that ARPES and QPI measurements in the nematic phase detect a peanut-shaped X pocket, but do not see the Y pocket [19–24]. The argument here is that for large enough Φ_{xy} , the Y pocket disappears, as its bottom moves above the Fermi level (Fig. 1(d)). A similar behavior has been obtained in monoclinic systems by allowing a non-zero interorbital d_{xz} - d_{xy} and d_{yz} - d_{xy} nematicity [25]. Within scenario A, it was argued [26] that the Y pocket is not observed, because in the nematic phase it becomes predominantly d_{xy} (the blue ellipse in Fig. 1(b)), and these excitations are less coherent than the ones for d_{xz} and d_{yz} fermions [27]. In this work we analyze the effect of nematicity on the superconducting state within both scenarios. We discuss the angular dependence of the superconducting gap, most notably on the hole pockets, and the behavior on the specific heat $C(T)$ at and below T_c .

Multi-orbital superconductivity in Fe-based materials in the absence of a nematic order has been extensively studied by many groups [2, 28–32]. A mixed orbital content of low-energy excitations implies that the pairing interaction necessarily has two orthogonal components: s -wave and d -wave, even when the interaction is local in the orbital basis. An s -wave interaction is attractive in the s^{+-} sub-channel (the sign of the gap on the hole pocket is opposite to that on electron X and Y pockets), a d -wave interaction is attractive in the $d_{x^2-y^2}$ sub-channel (the gap on the hole pocket scales as $\cos 2\theta$, where θ is the angle along the pocket, and has four nodes, while the gaps on the X and the Y pocket have opposite sign). In both cases, the gaps on the X and Y pockets are sign-preserving, but generally have minima at the points where d_{xz} (d_{yz}) orbital content vanishes. These minima can become nodes if d_{xy} orbitals contribute to superconductivity [11].

The pairing interaction in the s -wave and the d -wave channels is expressed in terms of dressed interactions

between hole and electron pockets: intra-orbital density-density interaction U_{he} , and inter-orbital pair-hopping interactions J_{he} and J_{ee} (see Sec III below). The terms U_{he} and J_{he} are enhanced by magnetic fluctuations with momenta near $(0, \pi)$ and $(\pi, 0)$ (the distances between the centers of the Γ and the X and the Y pockets, respectively), and J_{ee} is enhanced by magnetic fluctuations with momentum (π, π) (the distance between the X and the Y pockets). We follow earlier works [33,34] and assume that the dressed pairing interaction in the tetragonal phase is somewhat stronger in the s^{+-} channel. This implies that the pairing state without nematic order would be s^{+-} .

Superconductivity in the presence of a small nematic order $\Phi_{h,e}$ has been studied previously in Refs. [33–35]. The expected outcome is that a nematic order mixes s -wave and d -wave pairing channels, creating a mixed $s+d$ state. A general belief, coming from small $\Phi_{h,e}$ analysis is that in such a state the gap along the hole pocket is $\Delta_h(\theta) = \Delta_s + \Delta_d \cos 2\theta$, where θ is the angle along the pocket. The magnitude of Δ_d increases with Φ , and if one would extend the small Φ analysis to larger Φ , one would obtain that $\Delta_h(\theta)$ develops a deep minima and then accidental nodes. This reasoning has been applied to explain ARPES and STM data in FeSe [35, 36]. We argue that this is not necessarily the case because there is a second, competing effect of nematicity. Namely, a nematic order changes the orbital composition of the pockets (this phenomenon has been termed orbital transmutation [17]). This leads to two effects. First, the variable θ gets renormalized and becomes dependent on Φ_h . At large enough Φ_h , the dressed θ (called ϕ later in the paper) clusters near $\pm\pi/2$, depending on the sign of Φ_h , and the gap loses its angle dependence. Second, the ratio Δ_d/Δ_s becomes a non-linear function of Φ_h , and the ratio Φ_h/Φ_e . Furthermore, in some intervals of Φ_h/Φ_e it remains below one even at large Φ_h values. This prevents the appearance of the nodes even if the angular variation of the d -wave gap component is still a sizable one.

Our goal is to understand what happens at intermediate values of Φ , relevant to FeSe, in particular, whether there exists the range of Φ_h and Φ_h/Φ_e , where Δ_h has nodes. We show that this range exists, but is confined to near-equal interactions in s -wave and d -wave channels. Nevertheless, even if the gap does not have nodes, its angular variation follows the orbital content of the hole pocket and undergoes a strong evolution once the orbital content changes. For completeness, we also consider the case when the d -wave interaction is stronger than the one in the s^{+-} channel. In this case, the gap has 4 nodes at small $\Phi_{h,e}$ and no nodes at large $\Phi_{h,e}$, due to orbital transmutation. We show that the transformation of the nodal structure at intermediate $\Phi_{h,e}$ is rather involved, and for some Φ_e/Φ_h there exists an intermediate gap configuration with 8 nodes.

We next consider the behavior of the specific heat $C_v(T)$ at and below T_c . We analyze how the jump of $C_v(T)$ varies with the type of nematic order and whether the jump primarily comes from fermions from d_{xz} and d_{yz} orbitals, or there is a sizable contribution from the d_{xy} orbital. A similar issue has been recently studied [37] for KFe_2As_2 . There, d_{xy} orbital gives the dominant contribution to $C_v(T)$ in the normal state because of large mass of d_{xy} fermions, but contributes little to the jump of $C_v(T)$ and also to temperature dependence of $C_v(T)$ in a wide temperature region below T_c , because a superconducting gap on this orbital is inversely proportional to its mass and is much smaller than the ones on d_{xz} and d_{yz} orbitals. We analyze whether the same holds for FeSe, using the values of quasiparticle masses, extracted from ARPES. We find that the jump of the specific heat at T_c is smaller than in BCS theory for the same number of pockets, by the same reason as in KFe_2As_2 , d_{xy} fermions substantially contribute to $C_v(T)$ in the normal state but little to the jump of $C_v(T)$ at T_c . We decompose δC_v into contributions from different pockets and show that the largest contribution comes from fermions on a hole pocket in scenario A and from an electron pocket in scenario B. We analyze how δC_v evolves with nematic order and again find strong correlation with the orbital transmutation.

Finally, we address the issue of potential second transition to the new phase within the superconducting state. The argument here is that in a situation, when the attraction in the $d_{x^2-y^2}$ channel is comparable to that in the s^{+-} channel, a bi-quadratic coupling between s - and d -order parameters may turn the $s+d$ pairing state into an $s+ie^{i\eta}d$ state (the analog of a mixed $s+id$ state in the absence of nematicity). Such a state breaks Z_2 time-reversal symmetry, as the relative factor can be either i or $-i$. Recent specific heat measurements, $C_v(T)$, of FeSe [38–43] found an anomaly at $T \sim 1\text{K}$, which might indicate the emergence of $s+e^{i\eta}d$ order [34]. To verify the scenario, we vary the relative strength of the pairing interactions in s -wave and d -wave channels and analyze the Landau functional including both the bi-quadratic couplings between s - and d -gap components and the effect of orbital transmutation in the nematic phase. Although the orbital transmutation shrinks the parameter range of $s+e^{i\eta}d$ state, a transition into an $s+e^{i\eta}d$ state below T_c is still possible.

The structure of the paper is the following. In the

next Section we briefly discuss the electronic structure of FeSe. In Sec. III A we obtain the pairing interaction within scenario A, convert it into the band basis, and solve for the pairing gaps on hole and electron pockets. In Sec. III B we analyze the angular dependence of the gap on the hole pocket at various Φ_h and Φ_h/Φ_e . In Sec. III C we study temperature dependence of the gap below T_c . In Sec. IV we compute the jump of the specific heat at T_c within both scenarios and compare them to the available experimental data. We decompose the jump into contributions from different orbitals and study their relative strength. We also compute specific heat at $T < T_c$. In Sec. V we consider a putative transition into $s+e^{i\eta}d$ state. Finally, We present our conclusions in Sec. VI.

II. THE BAND HAMILTONIAN

As mentioned in the Introduction, we consider a two-dimensional 3 band/3 pocket model Hamiltonian with a hole pocket, centered at the Γ point of the BZ and two electron pockets, centered at $X = (0, \pi)$ and $Y = (\pi, 0)$ points of the Brillouin zone, respectively. For simplicity, we neglect the effect of spin-orbit coupling on the band dispersion. The hole pocket and the corresponding hole band is composed of d_{xz} and d_{yz} orbitals. The X -pocket/band is composed of d_{yz} and d_{xy} orbitals, and the Y -pocket/band is composed of d_{xz} and d_{xy} orbitals. We introduce two-component spinors $\psi_\Gamma = (d_{xz}, d_{yz})^T$ and $\psi_{X/Y} = (d_{yz/xz}, d_{xy})^T$ and write the kinetic energy H_0 as

$$H_0 = H_\Gamma + H_X + H_Y, \quad (3)$$

where each term is bilinear in spinors. For scenario A we introduce the nematic order Φ as the difference in the occupation of d_{xz} and d_{yz} orbitals, see Eq. (1). We define Φ on the hole pocket as Φ_h and on the electron pocket as Φ_e . The latter is the difference in the occupation of d_{xz} orbital on the Y pocket and d_{yz} orbital on the X pocket. For scenario B we additionally introduce a second component of a nematic order as the difference between occupations of d_{xy} orbitals on Y and X pockets, see Eq. (2).

A. Hole Pocket

The band Hamiltonian for the hole pocket H_Γ is [17, 33, 44, and 45]

$$H_\Gamma = \psi_\Gamma^\dagger \left[\left(\mu_h - \frac{\mathbf{k}^2}{2m_h} \right) \tau_0 - \left(\frac{b}{2} \mathbf{k}^2 \cos 2\theta_h - \Phi_h \right) \tau_3 - c \mathbf{k}^2 \sin 2\theta_h \tau_1 \right] \psi_\Gamma, \quad (4)$$

where θ_h is the polar angle for momentum \mathbf{k} , measured

from the k_x -direction in the anti-clockwise direction. We

set $c = -\frac{b}{2}$, which yields circular hole pockets in the tetragonal phase. The parameters of Eq. (4) are listed in Table I, and were obtained in Refs. [3,10] from fitting to ARPES data for FeSe at $k_z = \pi$. Diagonalizing Eq. (4), we obtain two dispersions. In the absence of nematicity, they give rise to the outer and the inner hole pockets, Fig. 3(a). At a finite $\Phi_h > \mu_h$, the inner hole pocket becomes very shallow and then disappears as the corresponding dispersion sinks below the Fermi level. For this reason, we neglect the inner hole band in our analysis of the low-energy physics.

The larger hole Fermi surface pocket survives at a finite Φ_h and becomes elliptical. The dispersion of the corresponding band is

$$\xi_h(\mathbf{k}) = \mu_h - \frac{\mathbf{k}^2}{2m_h} + \sqrt{\Phi_h^2 + b^2 \frac{\mathbf{k}^4}{4} - b\mathbf{k}^2 \Phi_h \cos 2\theta_h}, \quad (5)$$

see Fig. 3(b). The band operator h is a linear combination of fermionic operators from d_{xz} and d_{yz} operators:

$$h = \cos \phi_h d_{yz} + \sin \phi_h d_{xz}, \quad (6)$$

where the momentum label (\mathbf{k}) is implicit and ϕ_h is defined via

$$\cos 2\phi_h = \frac{b \frac{\mathbf{k}^2}{2} \cos 2\theta_h - \Phi_h}{\sqrt{\Phi_h^2 + b^2 \frac{\mathbf{k}^4}{4} - b\mathbf{k}^2 \Phi_h \cos 2\theta_h}}. \quad (7)$$

At $\Phi_h = 0$, $\phi_h = \theta_h$, and d_{yz} and d_{xz} fermions contribute to h with weights $|\langle d_{yz}|h\rangle|^2 = \cos^2 \theta_h$ and $|\langle d_{xz}|h\rangle|^2 = \sin^2 \theta_h$, simply related by $\pi/2$ rotation. At a non-zero Φ_h , ϕ_h becomes different from θ_h , and the weight of the two orbitals is no longer equal. At large Φ_h , $\cos 2\phi_h = -\text{sgn} \Phi_h$. Choosing for definiteness $\Phi_h > 0$, we find that $\phi_h = \pi/2$, hence the band operator h in Eq. (6) becomes entirely d_{xz} , i.e., the hole pocket becomes mono-orbital. This effect has been dubbed orbital transmutation [17 and 45]. The angular variation of $\cos 2\phi_h$ on the outer hole pocket for intermediate values of Φ_h is shown in Fig. 2(a). At $\Phi_h = \Phi_{cr} = bk_F^2/2 = \mu_h m_h b$, $\cos 2\phi_h$ along k_x -direction jumps discontinuously from +1 to -1 (yellow and green curves in Fig. 2(a)), and the orbital content jumps from a pure d_{yz} to a pure d_{xz} (see Fig. 2(b)). Because of that jump, the angular average of $\cos 2\phi_h$ and $\cos^2 2\phi_h$ along the hole Fermi surface, viewed as a function of Φ_h , becomes non-analytic at Φ_{cr} . In addition, at $\Phi \geq \Phi_{cr}$, the number of nodes of $\cos 2\phi_h$ on the Fermi surface increases from 4 to 8 (the green curve in Fig. 2(a)). We will show later that both features affect the structure of the superconducting gap function. For band parameters from Table I, $\Phi_{cr} \approx 7.6$ meV.

μ_h	$(2m_h)^{-1}$	b
13.6	473	529

TABLE I. Band Parameters for the hole pocket

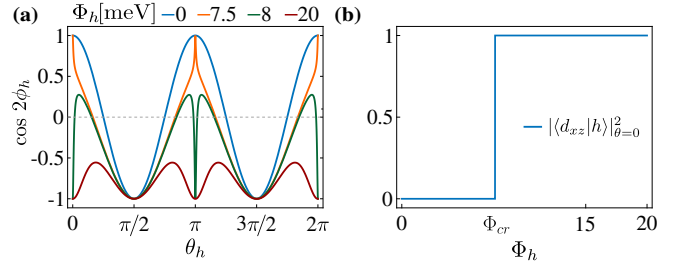


FIG. 2. (a) Angular variation of $\cos 2\phi_h$ along the hole Fermi pocket for selected values of Φ_h , (b) the d_{xz} orbital weight at $\theta_h = 0$ as a function of Φ_h .

B. X and Y Pockets

The electron pockets are described by the band Hamiltonian $H_{X/Y}$ [17, 33, 44, and 45].

$$H_{X/Y} = \psi_{X/Y}^\dagger \begin{pmatrix} A_{X/Y}^{(1)} & -iV_{X/Y} \\ iV_{X/Y} & A_{X/Y}^{(2)} \end{pmatrix} \psi_{X/Y}. \quad (8)$$

The diagonal elements are

$$A_{X/Y}^{(1)} = \frac{\mathbf{k}^2}{2m_1} - \mu_1 - \frac{a_1}{2} \mathbf{k}^2 \cos 2\theta_{X/Y} \pm \Phi_e, \quad (9)$$

$$A_{X/Y}^{(2)} = \frac{\mathbf{k}^2}{2m_3} - \mu_3 - \frac{a_3}{2} \mathbf{k}^2 \cos 2\theta_{X/Y}. \quad (10)$$

Here, \mathbf{k} is measured from $X = (\pi, 0)$ for the X pocket, and from $Y = (0, \pi)$ for the Y pocket and the upper (lower) sign corresponds to the X(Y)-pocket. θ_X (θ_Y) is the polar angle, measured with respect to $k_{x(y)}$ -direction for the X(Y) electron pocket in the anti-clockwise direction. Φ_e is the electron nematic order defined as, $\Phi_e = \langle d_{xz,Y}^\dagger d_{xz,Y} - d_{yz,X}^\dagger d_{yz,X} \rangle$. We choose $\Phi_e < 0$ (opposite in sign to Φ_h). The off-diagonal term $V_{X/Y}$ is defined as

$$V_X(k, \theta_X) = \sqrt{2}vk \sin \theta_X + \frac{p_1}{\sqrt{2}} k^3 \sin \theta_X (\sin^2 \theta_X + 3 \cos^2 \theta_X) - \frac{p_2}{\sqrt{2}} k^3 \sin \theta_X \cos 2\theta_X, \quad (11)$$

$$V_Y(k, \theta_Y) = -V_X(k, \theta_Y). \quad (12)$$

The band parameters of Eq. (8) are listed in Table II. We borrowed the numbers from Refs. [3,10], where these parameters have been extracted from ARPES data.

Diagonalizing Eq. (8) near the X point, we find that there is a single band that crosses the Fermi level in

μ_1	μ_3	$(2m_1)^{-1}$	$(2m_3)^{-1}$	a1	a3	v	p1	p2
19.9	39.4	1.4	186	136	-403	-122	-137	-11.7

TABLE II. Band Parameters for the electron pocket

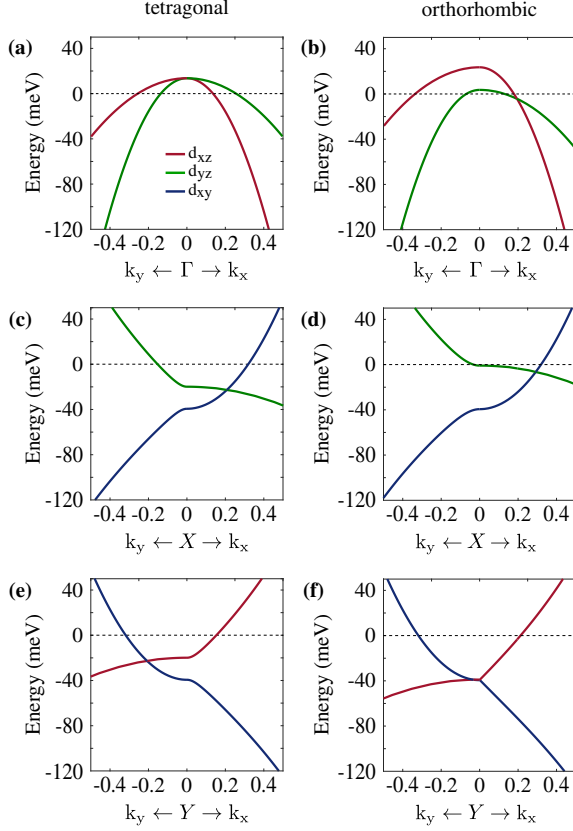


FIG. 3. Scenario A: Calculated band dispersion of the 1-Fe unit cell in tetragonal and orthorhombic phase, respectively, near (a-b) Γ -, (c-d) X- and (e-f) Y- points of the BZ, respectively. Fitting parameters are taken from Refs. [3,10]

both the tetragonal and the orthorhombic phase, see Fig. 3(c,d). The same holds near Y, Fig. 3(e,f). We only consider these bands and neglect the ones which are located fully below E_F . The dispersions of the two relevant bands are

$$\xi_{X/Y} = \frac{A_{X/Y}^{(1)} + A_{X/Y}^{(2)}}{2} + \sqrt{\left(\frac{A_{X/Y}^{(1)} - A_{X/Y}^{(2)}}{2}\right)^2 + V_{X/Y}^2}, \quad (13)$$

and the band operators e_X and e_Y , in terms of which $H_{X/Y} = \sum_{\mathbf{k}, \sigma} \xi_{X/Y}(\mathbf{k}) e_{X/Y, \mathbf{k}, \sigma}^\dagger e_{X/Y, \mathbf{k}, \sigma}$, are

$$e_X = -i \cos \phi_X d_{yz} + \sin \phi_X d_{xy}, \quad (14)$$

$$e_Y = i \cos \phi_Y d_{xz} + \sin \phi_Y d_{xy}, \quad (15)$$

where

$$\cos^2(\phi_{X/Y}) = \frac{1}{2} \left[1 + \frac{\frac{A_{X/Y}^{(1)} - A_{X/Y}^{(2)}}{2}}{\sqrt{\left(\frac{A_{X/Y}^{(1)} - A_{X/Y}^{(2)}}{2}\right)^2 + V_{X/Y}^2}} \right]. \quad (16)$$

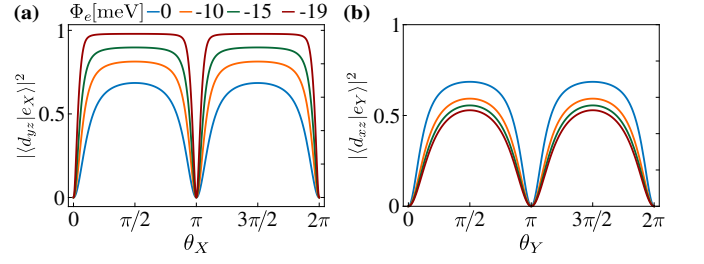


FIG. 4. The angular variation of orbital contents $|\langle d_{yz} | e_X \rangle|^2 = \cos^2 \phi_X$ on the X-pocket (a), and $|\langle d_{xz} | e_Y \rangle|^2 = \cos^2 \phi_Y$ on the Y-pocket (b) for a set of Φ_e .

The angular variation of the orbital $d_{yz/xz}$ content, $|\langle d_{yz/xz} | e_{X/Y} \rangle|^2 = \cos^2 \phi_{X/Y}$ on the Fermi surface is plotted in Fig. 4. Because of C_4 symmetry in the tetragonal phase, X and Y pockets have the same amount of d_{yz} and d_{xz} orbital content (blue lines in Fig. 4). With increasing Φ_e , the X pocket becomes more of d_{yz} character and deforms into a peanut, while the Y pocket becomes more of d_{xy} character as its d_{xz} content decreases. For our band parameters, X pocket splits into two smaller pocket once $|\Phi_e| \geq 19.9$ meV (the short axis of the peanut becomes zero). Below we limit Φ_e to be smaller than this value.

III. SUPERCONDUCTIVITY

A. Pairing Interaction

The pairing interaction for the model with local fermion-fermion interaction in the band basis has been discussed previously [33,34]. We include the following components of the interaction Hamiltonian, relevant to the pairing: intra-orbital density-density interaction between fermions on hole and electron pockets, U_{he} , and inter-orbital pair-hopping interaction between fermions on hole and electron pockets, J_{he} , and between the two electron pockets, J_{ee} . There are other pairing interactions, i.e., a repulsion within each pocket, but we restrict our consideration to these three as they are enhanced by magnetic fluctuations with momenta $(0, \pi)$, $(\pi, 0)$, and (π, π) . The interaction Hamiltonian reads

$$\begin{aligned} H_{\text{int}} = & U_{he} \sum_{\mathbf{k}, \mathbf{k}', \mu} d_{\mu, \mathbf{k}, \uparrow}^\dagger d_{\mu, -\mathbf{k}, \downarrow}^\dagger d_{\mu, -\mathbf{k}' + \mathbf{Q}_\mu, \downarrow} d_{\mu, \mathbf{k}' + \mathbf{Q}_\mu, \uparrow} \\ & + J_{he} \sum_{\mathbf{k}, \mathbf{k}', \mu \neq \nu} d_{\mu, \mathbf{k}, \uparrow}^\dagger d_{\mu, -\mathbf{k}, \downarrow}^\dagger d_{\nu, -\mathbf{k}' + \mathbf{Q}_\nu, \downarrow} d_{\nu, \mathbf{k}' + \mathbf{Q}_\nu, \uparrow} \\ & + J_{ee} \sum_{\mathbf{k}, \mathbf{k}', \mu \neq \nu} d_{\mu, \mathbf{k} + \mathbf{Q}_\mu, \uparrow}^\dagger d_{\mu, -\mathbf{k} + \mathbf{Q}_\mu, \downarrow}^\dagger d_{\nu, -\mathbf{k}' + \mathbf{Q}_\nu, \downarrow} d_{\nu, \mathbf{k}' + \mathbf{Q}_\nu, \uparrow} \\ & + h.c. \end{aligned} \quad (17)$$

We consider only the pairing interaction involving d_{xz} and d_{yz} fermions, i.e., assume that $\mu, \nu \in \{xz, yz\}$, and $\mathbf{Q}_{xz} = (0, \pi)$, $\mathbf{Q}_{yz} = (\pi, 0)$. The restriction to

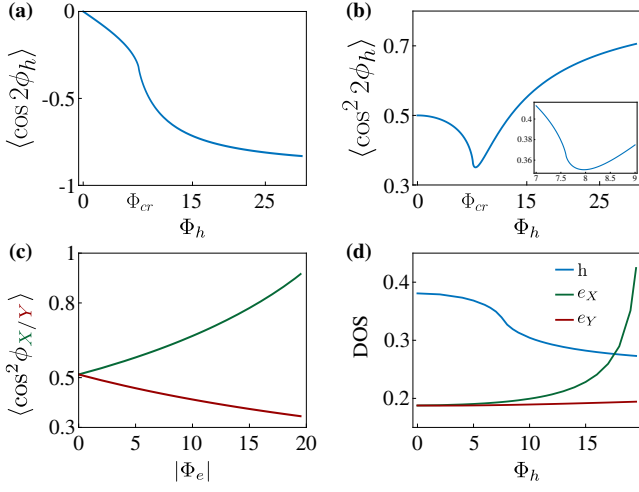


FIG. 5. Variation of the angular average of (a) $\langle \cos 2\phi_h \rangle$, (b) $\langle \cos^2 2\phi_h \rangle$, (c) $\langle \cos^2 \phi_X \rangle$ and $\langle \cos^2 \phi_Y \rangle$ on the hole and the electron pockets with the nematic order $\Phi_{h,e}$. The inset in (b) shows the zoom-in view of $\langle \cos^2 2\phi_h \rangle$ near Φ_{cr} . The non-analyticity is at $\Phi_{cr} \approx 7.6$ meV. (d) Variations of the density of state (DOS) on different pockets with Φ_h .

d_{xz} and d_{yz} orbitals is justified as d_{xy} -fermions have a larger mass [37]. To convert the interaction Hamiltonian, Eq. (17) from the orbital to the band basis we use

$$d_{xz,\mathbf{k}} = \sin \phi_h(\mathbf{k}) h_{\mathbf{k}}, \quad d_{xz,\mathbf{k}+\mathbf{Q}_{xz}} = \cos \phi_Y(\mathbf{k}) e_{Y,\mathbf{k}}, \quad (18)$$

$$d_{yz,\mathbf{k}} = \cos \phi_h(\mathbf{k}) h_{\mathbf{k}}, \quad d_{yz,\mathbf{k}+\mathbf{Q}_{yz}} = \cos \phi_X(\mathbf{k}) e_{X,\mathbf{k}}. \quad (19)$$

Substituting these into Eq. (17), we obtain the pairing

$$\begin{bmatrix} \Delta_1 \\ \Delta_2 \\ \Delta_3 \\ \Delta_4 \end{bmatrix} = \frac{1}{\lambda} \begin{bmatrix} 0 & 0 \\ 0 & 0 \\ -N_h \langle 1 + \alpha \cos 2\phi_h \rangle & -N_h \langle \cos 2\phi_h + \alpha \cos^2 2\phi_h \rangle \\ -N_h \langle 1 - \alpha \cos 2\phi_h \rangle & -N_h \langle \cos 2\phi_h - \alpha \cos^2 2\phi_h \rangle \end{bmatrix} \begin{bmatrix} -N_X \langle \cos^4 \phi_X \rangle & -N_Y \langle \cos^4 \phi_Y \rangle \\ -N_X \alpha \langle \cos^4 \phi_X \rangle & N_Y \alpha \langle \cos^4 \phi_Y \rangle \\ 0 & -\frac{J_{ee}}{U_s} N_Y \langle \cos^4 \phi_Y \rangle \\ -\frac{J_{ee}}{U_s} N_X \langle \cos^4 \phi_X \rangle & 0 \end{bmatrix} \begin{bmatrix} \Delta_1 \\ \Delta_2 \\ \Delta_3 \\ \Delta_4 \end{bmatrix}. \quad (24)$$

Here λ is the eigenvalue of the gap matrix defined as $\frac{1}{\lambda} = U_s \log(\frac{\Delta}{T})$, $\langle A \rangle$ defines the angular average of A over the corresponding Fermi surface pocket, and N_X , N_Y and N_h are the densities of states for the X , Y , and the Γ pocket, respectively. In Fig. 5(a,b,c), we show the variation of $\langle \cos 2\phi_h \rangle$, $\langle \cos^2 2\phi_h \rangle$, $\langle \cos^4 \phi_X \rangle$, and $\langle \cos^4 \phi_Y \rangle$ as a function of the nematic order $\Phi_{h,e}$. We find that $\langle \cos 2\phi_h \rangle$ and $\langle \cos^2 2\phi_h \rangle$ exhibit a kink like non analyticity near $\Phi_h = \Phi_{cr}$. In the Appendix we show that the singularities (non-analyticities) are $x \log(x)$, and $x^2 \log(x)$, where $x = \Phi_h / \Phi_{cr} - 1$. The densities of states also depend on $\Phi_{h,e}$, as we show them in the Fig. 5(d).

We numerically solve Eq. (24) and obtain T_c and find the gap structure $\Delta = (\Delta_1, \Delta_2, \Delta_3, \Delta_4)$ for the lead-

ing superconducting instability. In the tetragonal phase,

$$H_{\text{pair}} = \sum_{\mathbf{k}, \mathbf{p}} h_{\mathbf{k}, \uparrow}^\dagger h_{-\mathbf{k}, \downarrow}^\dagger \times \left[U_s (e_{X, -\mathbf{p}, \downarrow} e_{X, \mathbf{p}, \uparrow} \cos^2 \phi_X + e_{Y, -\mathbf{p}, \downarrow} e_{Y, \mathbf{p}, \uparrow} \cos^2 \phi_Y) + U_d \cos 2\phi_h (e_{X, -\mathbf{p}, \downarrow} e_{X, \mathbf{p}, \uparrow} \cos^2 \phi_X - e_{Y, -\mathbf{p}, \downarrow} e_{Y, \mathbf{p}, \uparrow} \cos^2 \phi_Y) \right] + J_{ee} \cos^2 \phi_X \cos^2 \phi_Y e_{X, \mathbf{k}, \uparrow}^\dagger e_{X, -\mathbf{k}, \downarrow}^\dagger e_{Y, -\mathbf{p}, \downarrow} e_{Y, \mathbf{p}, \uparrow} + h.c., \quad (20)$$

where, $U_s = \frac{U_{he} + J_{he}}{2}$ and $U_d = \frac{U_{he} - J_{he}}{2}$ are s - and d -wave components of the pairing interaction between the hole and the electron pockets. We use $\alpha = \frac{U_d}{U_s}$ to measure relative strength of this part of the interaction in the s -wave and the d -wave channels.

B. Gap Equation

We introduce the gap functions Δ_h on the hole pocket and Δ_X and Δ_Y on the electron pockets. The equations for Δ_h , Δ_X , and Δ_Y are obtained by solving 3×3 matrix equation. We present the BCS gap equations in Appendix (B), Eqs. (B1-B3). The solution of these gap equations is

$$\Delta_h = \Delta_1 + \Delta_2 \cos 2\phi_h, \quad (21)$$

$$\Delta_X = \Delta_3 \cos^2 \phi_X, \quad (22)$$

$$\Delta_Y = \Delta_4 \cos^2 \phi_Y. \quad (23)$$

At $T \approx T_c$, $\Delta_i (i = 1, \dots, 4)$ are the solutions of the matrix equation:

ing superconducting instability. In the tetragonal phase, $N_X = N_Y = N_e$ and $\langle \cos 2\phi_h \rangle = \langle \cos 2\theta_h \rangle = 0$. Then s^\pm -wave and d -wave pairing channels are decoupled. The eigenvalues of the gap matrix, Eq(24), are

$$\lambda_s = \lambda_0 \left[-\frac{J_{ee}}{U_s} + \sqrt{\left(\frac{J_{ee}}{U_s}\right)^2 + 8 \frac{N_h}{N_e \langle \cos^4 \phi_X \rangle}} \right], \quad (25)$$

$$\lambda_d = \lambda_0 \left[\frac{J_{ee}}{U_s} + \sqrt{\left(\frac{J_{ee}}{U_s}\right)^2 + 4 \frac{N_h}{N_e \langle \cos^4 \phi_X \rangle} \alpha^2} \right], \quad (26)$$

where $\lambda_0 = \frac{N_e \langle \cos^4 \phi_X \rangle}{2}$. For $J_{ee} = 0$, the gap function is either s -wave, for $\alpha < \sqrt{2}$, or d -wave, for $\alpha > \sqrt{2}$. For

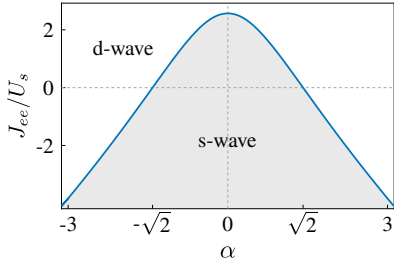


FIG. 6. Regions of *s*-wave and *d*-wave superconductivity according to the solution of Eq. (27) for different α and J_{ee} in the absence of nematicity.

$J_{ee} \neq 0$, superconductivity is *s*-wave when

$$\frac{J_{ee}}{U_s} < \sqrt{\frac{N_h}{2N_e \langle \cos^4 \phi_X \rangle}} \frac{(2 - \alpha^2)}{\sqrt{\alpha^2 + 2}}. \quad (27)$$

The phase diagram for Eq. 27 is shown in Fig. 6. We next move to the nematic phase. Now $\langle \cos 2\phi_h \rangle \neq 0$, and both Δ_1 and Δ_2 are non-zero for any α and J_{ee} .

To simplify the presentation, we neglect J_{ee} . Without nematicity, superconducting order is *s*-wave for $\alpha < \sqrt{2}$ and $\Delta_h = \Delta_1$. At small Φ (i.e., small Φ_h and Φ_e), $\phi_h \approx \theta_h$ and $\Delta_2 \propto \Phi$. This gives rise to $\Phi \cos 2\theta_h$ angular variation of Δ_h . If this was the only effect of nematicity, the angle variation would grow with Φ , and Δ_h would necessary develop a deep minima and then gap nodes. However, as Φ increases, ϕ_h deviates from θ_h due to orbital transmutation, and at large Φ becomes $\pi/2$ almost everywhere on the hole pocket. Then $\Delta_2 \cos 2\phi_h$ term becomes angle-independent, and the gap function on the hole pocket recovers a pure *s*-wave form. Besides, due to the same orbital transmutation, the magnitude Δ_2 becomes a non-linear function of Φ and not necessary exceeds Δ_1 even at large Φ .

A similar situation holds if $\alpha > \sqrt{2}$, when the superconducting order without nematicity is *d*-wave, $\Delta_h = \Delta_2 \cos 2\theta_h$. At a small Φ , the key effect of nematicity is an admixture of Δ_1 . At large Φ , $\theta_h \rightarrow \phi_h \approx \pi/2$, and the nodes disappear.

The questions, which we address below are (i) whether for $\alpha < \sqrt{2}$ the nodes in Δ_h develop at intermediate Φ_h and (ii) how the nodes in Δ_h disappear for $\alpha > \sqrt{2}$ as Φ_h increases. To address these issues we solve the gap equations for different α at various Φ_h and Φ_h/Φ_e . We show the results in Figs. 7-11. Before we discuss these results, several general observations are in order. According to Eq. (22), Δ_h has a node at an angle θ_0 if

$$\cos 2\phi_h(\theta_0, \Phi_h) = -\frac{\Delta_1}{\Delta_2}. \quad (28)$$

The ratio Δ_2/Δ_1 depends on Φ_h, Φ_e , and on α . Obviously, the nodes are possible only if $|\Delta_2/\Delta_1| > 1$. Shrinking the angular variation of $\cos 2\phi_h$ at $\Phi_h > \Phi_{cr}$ puts additional restriction on Δ_2/Δ_1 for the nodes to appear.

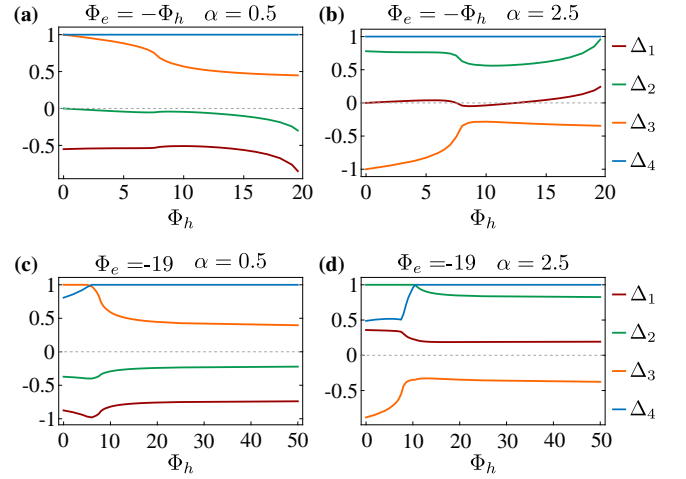


FIG. 7. Variations of the gap amplitudes $\Delta = (\Delta_1, \Delta_2, \Delta_3, \Delta_4)$ with the nematic order $\Phi_{e,h}$ and interaction ratio α for: (a) $\alpha = 0.5$, $\Phi_h = -\Phi_e$, (b) $\alpha = 2.5$, $\Phi_h = -\Phi_e$, (c) $\alpha = 0.5$, $\Phi_e = -19$ meV, (d) $\alpha = 2.5$, $\Phi_e = -19$ meV.

Further, the number of possible nodes changes between $\Phi_h < \Phi_{cr}$ and $\Phi_h > \Phi_{cr}$. In the first case, the gap functions at $\theta = 0$ and $\frac{\pi}{2}$ are $\Delta_1 + \Delta_2$ and $\Delta_1 - \Delta_2$, respectively. When $|\Delta_2/\Delta_1| > 1$, the two have opposite signs, hence there have to be an odd number of nodes between 0 and $\frac{\pi}{2}$; the total number of nodes is then 4, 12, 20, ... For $\Phi_h > \Phi_{cr}$, $\Delta_h(\theta)$ at $\theta = 0$ and $\pi/2$ become the same $\Delta_1 - \Delta_2$ due to orbital transmutation. Then, there have to be an even number of nodes between 0 and $\pi/2$, hence the total number of nodes is 0, 8, 16, ...

In our case, we find (see Appendix for details)

$$\frac{\Delta_2}{\Delta_1} = 2\alpha \frac{g + \alpha \langle \cos 2\phi_h \rangle}{(1 - \alpha^2 \langle \cos^2 2\phi_h \rangle) + D}, \quad (29)$$

where

$$g = g(\Phi_e) = \frac{N_X \langle \cos^4 \phi_X \rangle - N_Y \langle \cos^4 \phi_Y \rangle}{N_X \langle \cos^4 \phi_X \rangle + N_Y \langle \cos^4 \phi_Y \rangle}, \quad (30)$$

and

$$D = \left[4\alpha^2 (\langle \cos 2\phi_h \rangle^2 - \langle \cos^2 2\phi_h \rangle) (1 - g^2) + (1 + 2g\alpha \langle \cos 2\phi_h \rangle + \alpha^2 \langle \cos^2 2\phi_h \rangle)^2 \right]^{1/2}. \quad (31)$$

The function $g(\Phi_e)$ measures the asymmetry between X and Y pockets at a non-zero Φ_e . We find that it increases roughly linearly with $|\Phi_e|$.

We now discuss the results. In Fig. 7(a,c) we show Δ_i for $\alpha = 0.5$ and in (b,d) for $\alpha = 2.5$, when the primary order is *s*-wave and *d*-wave, respectively. We see that for $\alpha = 0.5$, the magnitude of the *s*-wave component Δ_1 far exceeds Δ_2 of the *d*-wave component, i.e., the gap remains an *s*-wave with a small admixture of *d*-wave.

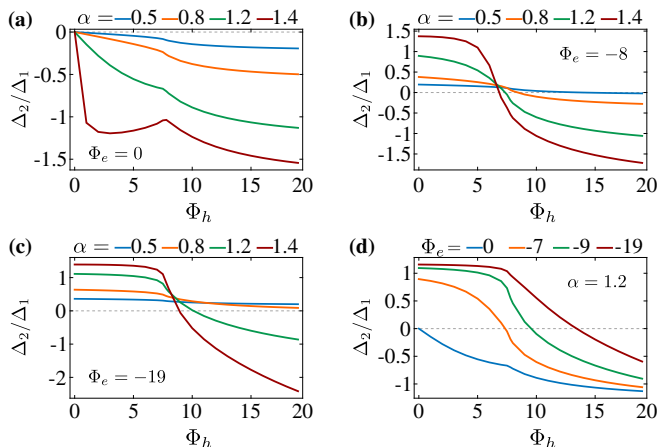


FIG. 8. The variation of Δ_2/Δ_1 with Φ_h for different interaction ratios α for a fixed electron nematic order (a) $\Phi_e = 0$ meV, (b) $\Phi_e = -8$ meV, and (c) $\Phi_e = -19$ meV. In (d) we fix $\alpha = 1.2$ and plot Δ_2/Δ_1 with Φ_h for different values of electron nematic order Φ_e .

For $\alpha = 2.5$, the situation is opposite – the gap remains predominantly d -wave with a small admixture of an s -wave. In both cases therefore, the effect of nematicity is rather weak, even when Φ_h is large.

In Fig. (8) we plot Δ_2/Δ_1 as a function of Φ_h for various Φ_e and $\alpha < \sqrt{2}$. We see that when α is not close to $\sqrt{2}$, then $|\Delta_2/\Delta_1| < 1$ for any Φ_h and Φ_e . As a consequence, there are no nodes in the gap function. This agrees with Fig. 7. However, for $\alpha \leq \sqrt{2}$, we find intervals of $\Phi_h < \Phi_{cr}$, where $|\Delta_2/\Delta_1| > 1$. This holds, e.g., for $\alpha = 1.4$ and $\Phi_e = 0$ (dark red curve in Fig. 8(a)). By our generic reasoning, there must be 4 nodes. The same holds for the same α and sizable Φ_e (see Figs. 8(b,c)). The only difference is that for $\Phi_e = 0$, the 4 nodes are near k_x -direction, while for sizable Φ_e they are near k_y -direction.

Next, we see from Fig. 8 that the ratio $|\Delta_2/\Delta_1|$ evolves around $\Phi_h = \Phi_{cr}$ and even changes sign for sizable Φ_e . For larger Φ_h we again have $|\Delta_2/\Delta_1| > 1$ for $\alpha \leq \sqrt{2}$. However, this no longer guarantees the existence of the nodes as by our general reasoning above their number can be zero. We will see that this is what happens – the nodes do not develop despite $|\Delta_2/\Delta_1| > 1$ because ϕ_h clusters around $\pi/2$.

In Fig. 9 we mark the boundaries of $|\Delta_2/\Delta_1|$ on the (Φ_h, Φ_e) plane at a fixed $\alpha = 1.2$. The area of the "corner" regions, where $|\Delta_2/\Delta_1| > 1$, increases when α approaches $\sqrt{2}$. As we mentioned, the nodes only develop in the left upper grayish colored corner, where $\Phi_h < \Phi_{cr}$. In Fig. 10 we plot the gap function $\Delta_h(\theta_h)$. We find 4 different scenarios how nodes can appear/disappear when one varies Φ_h at a fixed value of Φ_e and α slightly below critical $\sqrt{2}$. Here, we further set $\alpha = 1.4$.

1. In Fig. 10(a) we set $\Phi_e = 0$. There are no nodes at $\Phi_h = 0$ in agreement with Fig. 8(a). At $\Phi_h \approx 1$ meV, 4 nodes appear near the k_x -direction. They

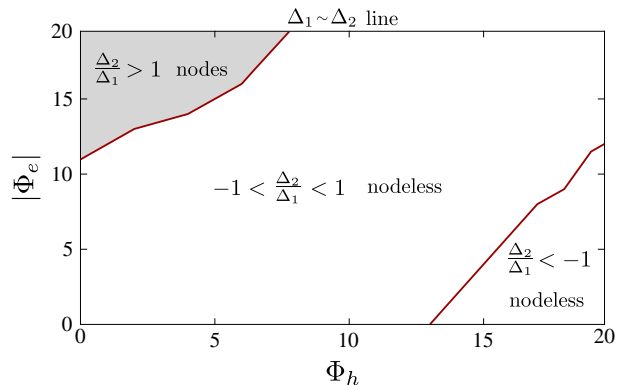


FIG. 9. The variation of Δ_2/Δ_1 as a function of Φ_h and Φ_e . We set $\alpha = 1.2$ in this plot.

exist up to $\Phi_h \leq \Phi_{cr}$ and disappear at larger Φ_h . In the node count, the number of nodes changes with Φ_h as $0 \rightarrow 4 \rightarrow 0$.

2. In Fig. 10(b) we set $\Phi_e = -1$ meV. In this case there are 4 nodes near k_y -direction already for $\Phi_h = 0$. As Φ_h increases, the 4 nodes disappear at $\Phi_h \sim 1$ meV due to non-monotonic behavior of Δ_2/Δ_1 , like in Fig. 8(b,c). As Φ_h increases further, 4 nodes reappear, now near k_x -direction, at $\Phi_h \sim 3$ meV. These nodes then disappear at $\Phi_h \leq \Phi_{cr}$. In this case, the number of nodes changes with Φ_h as $4 \rightarrow 0 \rightarrow 4 \rightarrow 0$.
3. In Fig. 10(c) we set $\Phi_e = -7$ meV. In this case, at small Φ_h there are 4 nodes near k_y -direction. These nodes disappear at some $\Phi_h \leq \Phi_{cr}$. In this case, number of nodes changes with Φ_h as $4 \rightarrow 0$
4. In Fig. 10(d) we set $\Phi_e = -19$ meV. In this case, there are 4 nodes near k_y -direction for all $\Phi_h \leq \Phi_{cr}$. For $\Phi_h > \Phi_{cr}$, the number of nodes first increases from 4 to 8, because the gap function along the k_x - and the k_y -direction becomes nearly the same and has to cross zero twice. As Φ_h increases further, the 8 nodes disappear due to clustering of ϕ_h near $\pi/2$. In this case, the number of nodes changes with Φ_h as $4 \rightarrow 8 \rightarrow 0$.

For $\alpha > \sqrt{2}$, superconducting order in the tetragonal phase is d -wave with 4 nodes on the hole pocket. With increasing nematic order the nodes disappear due to orbital transmutation either because Δ_1 becomes larger than Δ_2 or Δ_2 remains larger than Δ_1 , but ϕ_h clusters around $\pi/2$. In Fig. 11 we show the results for Δ_h at two values of $\alpha > \sqrt{2}$. For $\alpha = 1.45$, the nodes Δ_h disappear because Δ_1 becomes larger than Δ_2 . This happens at $\Phi_h < \Phi_{cr}$, i.e., well before ϕ_h starts clustering near $\pi/2$. In this case, the number of nodes changes with Φ_h as $4 \rightarrow 0$. For $\alpha = 2.5$ Δ_2 remains larger than Δ_1 , and the nodes disappear at $\Phi_h > \Phi_{cr}$ due to clustering of ϕ_h . We see from the Figure that in this case the number of

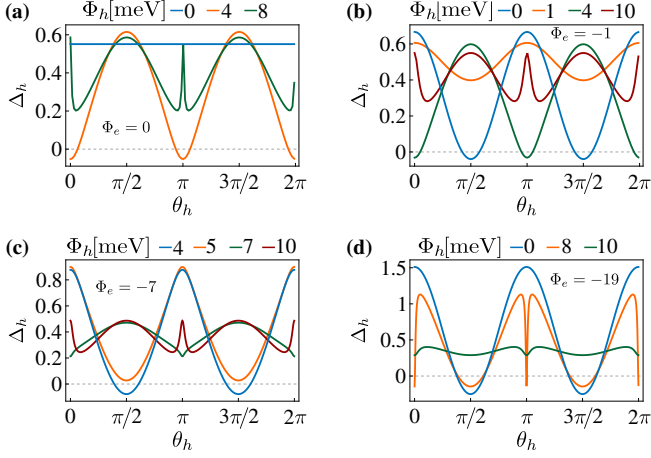


FIG. 10. The angular variation of $\Delta_h(\theta_h)$ with θ_h for various values of Φ_h at (a) $\Phi_e = 0$ meV, (b) $\Phi_e = -1$ meV, (c) $\Phi_e = -7$ meV, and (d) $\Phi_e = -19$ meV. We set $\alpha = 1.4$

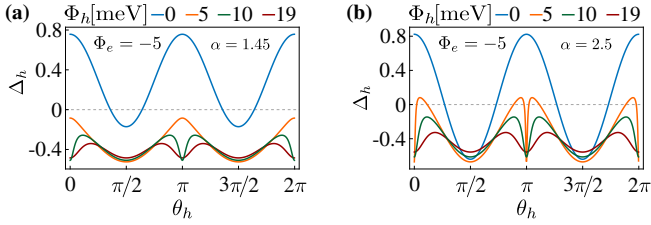


FIG. 11. Angular variation of $\Delta_h(\theta_h)$ at selected values of Φ_h for (a) $\alpha = 1.45$ and (b) $\alpha = 2.5$. We set $\Phi_e = -5$ meV.

nodes changes with Φ_h as $4 \rightarrow 8 \rightarrow 0$. (4 on a blue line, 8 on a orange, and 0 on green and red lines). A nodeless gap deep in orthorhombic phase for $\alpha > \sqrt{2}$ is consistent with RPA calculations of Ref. [11].

Note that the results for a non-zero J_{ee} are quite similar, only the value of α near which the system develops nodes coming out of an s -wave superconductor at $\Phi = 0$ shifts from $\alpha = \sqrt{2}$.

C. Temperature dependence of gap

In this section we obtain the temperature dependence of $\Delta_i(T)$ near the superconducting transition. We will use the result for $\Delta_i(T)$ in the next section, where we compute the jump of the specific heat at T_c . We assume that the ratios Δ_i/Δ_j do not change substantially with temperature and parametrize four gap functions as

$$\Delta(T) = \Delta_0(T) (\Delta_1, \Delta_2, \Delta_3, \Delta_4) = \Delta_0(T) \mathbf{\Delta}, \quad (32)$$

where $\mathbf{\Delta} = (\Delta_1, \Delta_2, \Delta_3, \Delta_4)$ are the same (up to an overall factor) as we obtained in Sec. III B by solving the linearized gap equations (24). We normalize $\mathbf{\Delta}$ by setting its largest component equal to 1. To simplify the presentation, we again first assume $J_{ee} = 0$ and then present the results for a non-zero J_{ee} .

The non-linear equation for the gap on the hole pocket is

$$\begin{aligned} & \Delta_1 + \Delta_2 \cos 2\phi_h \\ &= - \left[\Delta_3 (U_s + U_d \cos 2\phi_h) \int_{\mathbf{p}} \frac{\tanh(\frac{E_X}{2T})}{2E_X} \cos^4 \phi_X \right. \\ & \quad \left. + \Delta_4 (U_s - U_d \cos 2\phi_h) \int_{\mathbf{p}} \frac{\tanh(\frac{E_Y}{2T})}{2E_Y} \cos^4 \phi_Y \right], \quad (33) \end{aligned}$$

where $E_X = \sqrt{\xi_x^2 + \Delta_3^2 \Delta_0^2(T)}$, $E_Y = \sqrt{\xi_y^2 + \Delta_4^2 \Delta_0^2(T)}$. Multiplying Eq. (33) by $\Delta_1 + \Delta_2 \cos 2\phi_h$, averaging over the hole Fermi surface pocket, and expanding the r.h.s. to order $\Delta_0^2(T)$ as

$$\begin{aligned} & \int_{\mathbf{p}} \frac{\tanh(\frac{E_{X/Y}}{2T})}{2E_{X/Y}} \cos^4 \phi_{X/Y}(\mathbf{p}) = \\ & N_{X/Y} \left(\log \frac{\Lambda}{T} \langle \cos^4 \phi_{X/Y} \rangle - K \Delta_3^2 \frac{\Delta_0^2}{T_c^2} \langle \cos^8 \phi_{X/Y} \rangle \right) + O(\Delta_0^4), \quad (34) \end{aligned}$$

where $K = \frac{7\zeta(3)}{8\pi^2}$, we obtain

$$\begin{aligned} & N_h \log \frac{\Lambda}{T_c} \langle (\Delta_1 + \Delta_2 \cos 2\phi_h)^2 \rangle = \\ & \log \frac{\Lambda}{T} [N_X \Delta_3^2 \langle \cos^4 \phi_X \rangle + N_Y \Delta_4^2 \langle \cos^4 \phi_Y \rangle] \\ & - K \frac{\Delta_0(T)^2}{T_c^2} [N_X \Delta_3^4 \langle \cos^8 \phi_X \rangle + N_Y \Delta_4^4 \langle \cos^8 \phi_Y \rangle]. \quad (35) \end{aligned}$$

Multiplying the Eq. (B4) by $\Delta_1 + \Delta_2 \cos 2\phi_h$, averaging over the hole Fermi surface pocket, and using Eqs.(B5)-(B6), we obtain the relation

$$\begin{aligned} & N_h \langle (\Delta_1 + \Delta_2 \cos 2\phi_h)^2 \rangle \\ &= (N_X \Delta_3^2 \langle \cos^4 \phi_X \rangle + N_Y \Delta_4^2 \langle \cos^4 \phi_Y \rangle), \quad (36) \end{aligned}$$

Approximating $\log \frac{\Lambda}{T} \approx \log \frac{\Lambda}{T_c} + \frac{T_c - T}{T_c}$ and using Eq. (36), we obtain from (35)

$$\Delta_0(T)^2 = \frac{T_c(T_c - T)}{K} \frac{N_X \Delta_3^2 \langle \cos^4 \phi_X \rangle + N_Y \Delta_4^2 \langle \cos^4 \phi_Y \rangle}{N_X \Delta_3^4 \langle \cos^8 \phi_X \rangle + N_Y \Delta_4^4 \langle \cos^8 \phi_Y \rangle}. \quad (37)$$

We recall that Δ_3 and Δ_4 are functions of Φ_h , Φ_e and α . For $J_{ee} \neq 0$, the same procedure yields

$$\Delta_0(T)^2 = \frac{T_c(T_c - T)}{K} \frac{N_X \Delta_3^2 \langle \cos^4 \phi_X \rangle + N_Y \Delta_4^2 \langle \cos^4 \phi_Y \rangle + 2 \frac{J_{ee}}{\lambda} N_X N_Y \Delta_3 \Delta_4 \langle \cos^4 \phi_X \rangle \langle \cos^4 \phi_Y \rangle}{N_X \Delta_3^4 \langle \cos^8 \phi_X \rangle + N_Y \Delta_4^4 \langle \cos^8 \phi_Y \rangle + \frac{J_{ee}}{\lambda} N_X N_Y \Delta_3 \Delta_4 (\Delta_3^2 \langle \cos^8 \phi_X \rangle \langle \cos^4 \phi_Y \rangle + \Delta_4^2 \langle \cos^8 \phi_Y \rangle \langle \cos^4 \phi_X \rangle)}, \quad (38)$$

where λ is the largest eigenvalue of Eq. (24).

IV. SPECIFIC HEAT

In this section we examine the specific heat jump at T_c and its band-resolved composition, as a function of nematicity for scenarios A and B. In the mean-field approximation the specific heat is the sum of contributions from Γ , X and Y pockets:

$$C_v = \sum_{i=h,X,Y} \int_{\mathbf{k}} \left(\frac{E_i^2(\mathbf{k})}{2T^2} - \frac{1}{4T} \frac{\partial |\Delta_i(\mathbf{k})|^2}{\partial T} \right) \frac{1}{\cosh^2 \left(\frac{E_i(\mathbf{k})}{2T} \right)}. \quad (39)$$

The first term in the r.h.s of Eq. (39) is the normal state contribution at $T = T_c + 0^+$. Evaluating the k-integral we obtain

$$C_v = \frac{2}{3} \pi^2 T_c (N_h + N_X + N_Y). \quad (40)$$

The second term in the r.h.s of Eq. (39) accounts for the jump of ΔC_v at T_c . It is equal to

$$\begin{aligned} \Delta C_v &= -\frac{1}{4T_c} \sum_{i=h,X,Y} \int_{\mathbf{k}} \frac{1}{\cosh \left(\frac{\xi_i(\mathbf{k})}{2T_c} \right)^2} \frac{d}{dT} \Delta_i(\theta)^2 \\ &= -\sum_{i=h,X,Y} N_i \int_0^{2\pi} \frac{d\theta}{2\pi} \frac{d}{dT} \Delta_i(\theta)^2. \end{aligned} \quad (41)$$

Substituting the results for the gap functions, we find that

$$\begin{aligned} \Delta C_v &= -\frac{d}{dT} \Delta_0(T)^2 \left[N_h \langle (\Delta_1 + \Delta_2 \cos 2\phi_h)^2 \rangle \right. \\ &\quad \left. + N_X \Delta_3^2 \langle \cos^4 \phi_X \rangle + N_Y \Delta_4^2 \langle \cos^4 \phi_Y \rangle \right] \\ &= \Delta C_v^h + \Delta C_v^X + \Delta C_v^Y. \end{aligned} \quad (42)$$

Setting $J_{ee} = 0$ and using Eq. (36), we find that $\Delta C_v^h = \Delta C_v^X + \Delta C_v^Y$. Using Eqs.(36,37,42), we find

$$\frac{\Delta C_v}{C_v} = 1.43 \frac{2N_h^2 \langle \Delta_h(\theta)^2 \rangle^2}{N (N_X \Delta_3^4 \langle \cos^8 \phi_X \rangle + N_Y \Delta_4^4 \langle \cos^8 \phi_Y \rangle)}, \quad (43)$$

where 1.43 is the BCS result for a single band superconductor, and $N = N_h + N_X + N_Y$. Without a nematic order, the ratio would be

$$\left(\frac{\Delta C_v}{C_v} \right)_{\Phi=0} = 1.43 \frac{2}{1 + \frac{N_h}{2N_e}} \frac{\langle \cos^4 \phi_X \rangle^2}{\langle \cos^8 \phi_X \rangle}. \quad (44)$$

If the electron pockets would consist solely of d_{xz} and d_{yz} fermions, we would obtain $\Delta C_v/C_v|_{\Phi=0} = 2.86/(1 + N_h/(2N_e))$. For the parameters from Tables (I-II) this yields $\Delta C_v/C_v|_{\Phi=0} = 1.42$. In presence of the d_{xy} orbital, however, $\Delta C_v/C_v|_{\Phi=0} \approx 1.09$. The smallness comes from the fact that relatively heavy d_{xy} band contributes to $C_v(T)$ in the normal state, but not to ΔC_v . This is similar to the case of KFe_2As_2 (Ref³⁷).

A. Specific heat jump at T_c for scenario A

The effect of nematicity on the specific heat jump is involved because N_i , c_i , and the coherence factors $\cos \phi_i$, all vary with it. In Fig. 12, we plot $\Delta C_v/C_v$ as a function of Φ_h for various values of Φ_e and representative $\alpha = 0.5$ and 2.5, chosen to be smaller and larger than $\sqrt{2}$. For $\alpha = 0.5$, we expect from Eq. (43) that $\Delta C_v/C_v \approx \Delta_1^4$, and we verified that the behavior of $\Delta C_v/C_v$ matches the behavior of Δ_1^4 with Δ_1 from Fig. 7(a).

For $\alpha = 2.5$, we expect $\Delta C_v/C_v \sim \Delta_2^4$, and the behavior of $\Delta C_v/C_v$ matches the behavior of Δ_2^4 with Δ_2 from Fig. 7(b). In both cases, we see that $\Delta C_v/C_v$ is generally around one, but increases with Φ_h . Viewed as a function of Φ_h , $\Delta C_v/C_v$ displays a kink like non-analyticity at $\Phi_h = \Phi_{cr}$ and, moreover, is non-monotonic at $\alpha = 2.5$. The non-monotonic behavior for this α is clearly visible in Fig. 12(d), where we plot $\Delta C_v/C_v$ vs. Φ_h for various Φ_e . Fig. 12(c) shows that it also holds at $\alpha = 0.5$, for large enough $|\Phi_e|$. At large $|\Phi_e|$ and even larger Φ_h , $\Delta C_v/C_v$ saturates. The reason is that for such Φ , the Y pocket mostly of d_{xy} character and the X pocket is mostly of d_{yz} character, hence $\langle \cos^a \phi_Y \rangle \ll 1$ and $\langle \cos^a \phi_X \rangle \approx 1$, where $a = 4, 8$. Then $\Delta C_v/C_v \sim N_X/(N_h + N_X + N_X)$ and N_X is the largest, see Fig. 5(d). Note that for large $|\Phi_e| = 19$ meV, $\Delta C_v/C_v$ is 1.5 – 1.6.

For $\alpha \approx \sqrt{2}$, the behavior of $\Delta C_v/C_v$ vs Φ_h is intermediate between the ones at $\alpha = 0.5$ and $\alpha = 2.5$.

We also plot in Fig. 12(a,b) the band resolved contributions from hole and electron pockets. We see that the largest contribution to the jump comes from the hole pocket. $\Delta C_v^h/C_v$ is non-analytic at Φ_{cr} and gives rise to non-analyticity in the full $\Delta C_v/C_v$.

B. Specific heat jump at T_c for scenario B

Below we present the results for the specific heat jump and its decomposition into contributions from different bands for the scenario B, when there is additional contribution Φ_{xy} , Eq. (2). This contribution splits the dispersions of d_{xy} fermions on X and Y pocket. We choose

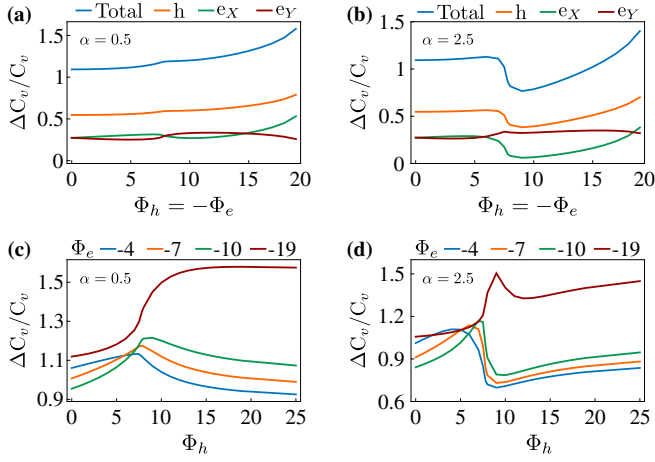


FIG. 12. The variation of the scaled specific heat jump $\frac{\Delta C_v}{C_v}$ with hole nematic order Φ_h for (a,c) $\alpha = 0.5$ and (b,d) $\alpha = 2.5$. We set $\Phi_e = -\Phi_h$ in (a) and (b). In (c) and (d), we choose a set of values for $\Phi_e = \{-4, -7, -10, -19\}$ meV.

the sign and magnitude of Φ_{xy} such that the bottom of the Y -band moves above the chemical potential, i.e., Y pocket disappears in the nematic phase. To simplify calculations, we adopt the "antisymmetric approach" of Ref. [11] and introduce Φ_{xy} nematic order only for d_{xy} fermions on the Y pocket, as $2\Psi_Y\Phi_{xy}\Psi_Y$ with Ψ_Y from Eq. (8). Appropriate parameters to fit the band structure, available from ARPES experiments, in this scenario are given in the supplementary of Ref. [11] and yield the Fermi surface shown in panel (d) of Fig. 1(d) and in the right inset in Fig. 14(c). The corresponding band dispersions at Γ -, X - and Y -points is shown in Fig. 13.

We solve the full non-linear gap equations (B1-B3), substitute the results into Eq. (39) and obtain the specific heat.

In Fig. 14(a) we show the total specific heat C_V (solid-blue) as well as the band resolved contributions from the Γ , X and Y pocket (solid yellow, green and orange, respectively). For definiteness we set $\Phi_{xy} = 45$ meV, $\alpha = 0.5$ and $J_{eh} = J_{ee}$ ($= U_{eh}/3$). We adjusted U_{eh} to match experimental $T_c \sim 10$ K. Observe that both Γ - and X -pocket contribute substantially to the specific heat jump, with the contribution from Y pocket almost vanishes. The largest contribution comes from the X pocket. This differs from the result for scenario A, but the difference is largely due to different parameters, as we verified.

A more substantial difference is actually for the specific heat in the normal state. In scenario A d_{xy} fermions from both X and Y pocket contribute to $C_v(T)$ above T_c . In scenario B, d_{xy} fermions from Y are gapped, and only d_{xy} fermions from X contribute. As a result, the normal state $C_v(T)$ is reduced in scenario B compared to A, while ΔC_v at T_c remains the same as only d_{xz} and d_{yz} fermions contribute to the jump. As the consequence, $\Delta C_v/C_v$ is larger in scenario B than in scenario A. We

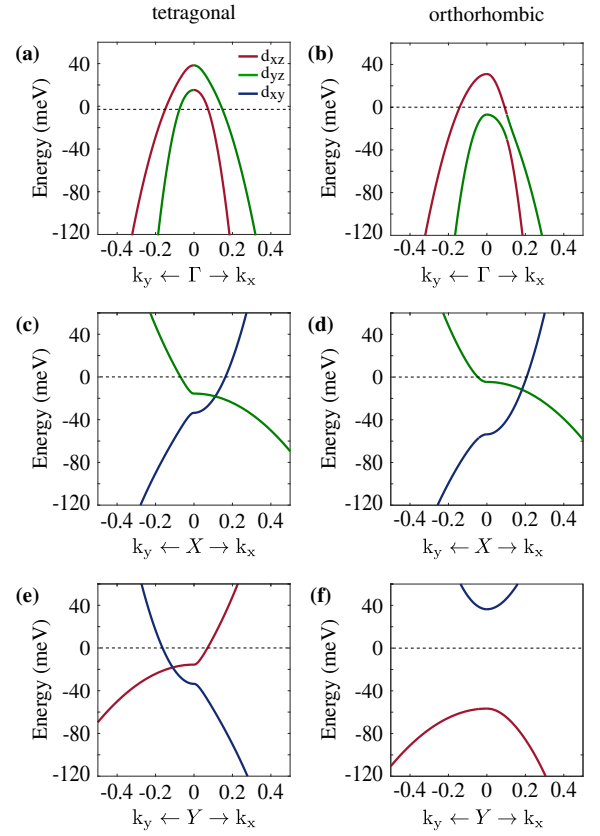


FIG. 13. Scenario B: Calculated band dispersion of the 1-Fe unit cell in tetragonal and orthorhombic phase, respectively, near (a-b) Γ -, (c-d) X - and (e-f) Y -point. Fitting parameters taken from Ref. [11]. Note that the d_{xy} dominated Y -band is fully located above the Fermi level in (f).

show this explicitly where we plot $\Delta C_v/C_v$ as a function of Φ_{xy} that drives the system between scenario A and scenario B. We see that $\Delta C_v/C_v$ is roughly a constant at small Φ_{xy} , when scenario A is valid. It then rapidly increases and saturates at a larger value at large Φ_{xy} , when scenario B is valid.

C. Comparison between scenario A, B and experiments

Specific heat measurements in FeSe [38–42, 46–50] consistently reveal that $\Delta C_v/C_v \approx 1.65$. This is larger than the BCS result for a single band superconductor, $\Delta C_v/C_v \approx 1.43$. A larger $\Delta C_v/C_v$ is often associated with the effects beyond BCS [51,52]. However, earlier works [53–58] have found that in a multi-band system $\Delta C_v/C_v$ can be either larger or smaller than the BCS value already within BCS approximation. In our analysis, we obtain $\Delta C_v/C_v$ around one in scenario A for small Φ_e and Φ_h , but larger $\Delta C_v/C_v \sim 1.5 - 1.6$ for larger $\Phi_h \sim |\Phi_e| \leq 20$ meV. Within scenario B, $\Delta C_v/C_v$ is always larger than in the scenario A because the nor-

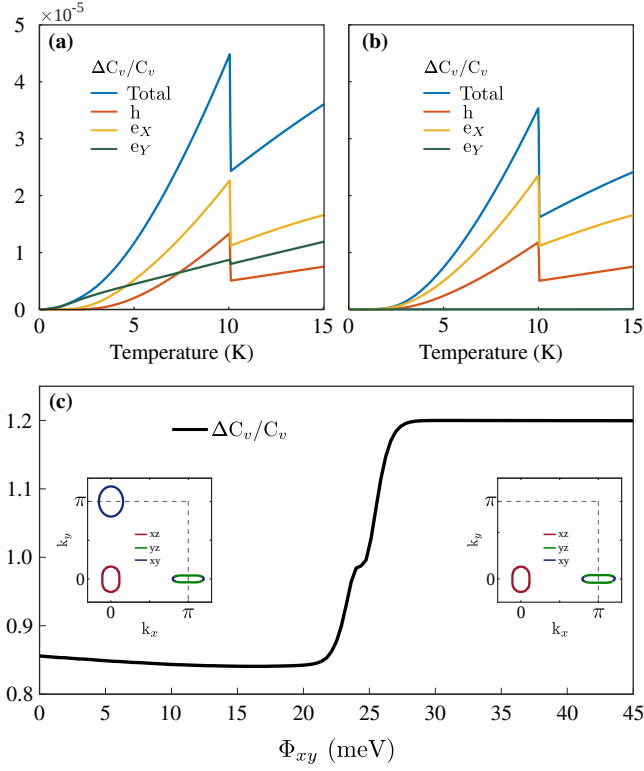


FIG. 14. The total and band resolved specific heat calculated for (a) scenario A ($\Phi_{xy} = 0$) and (b) scenario B ($\Phi_{xy} = 45$ meV); (c) $\Delta C_v/C_v$ as a function of Φ_{xy} . For small (large) Φ_{xy} scenario A (B) is valid. Left inset: Fermi surface for $\Phi_{xy} = 0$. Right inset: Fermi surface for $\Phi_{xy} = 45$ meV.

mal state contribution is smaller. Then the experimental $\Delta C_v/C_v \sim 1.65$ can be reproduced already at smaller $\Phi_{h,e}$. In summary, the specific heat jump can be reproduced within both scenarios, but the parameter space is somewhat larger in scenario B.

V. SPECIFIC HEAT NEAR A POSSIBLE TRANSITION INTO AN $s + e^{i\eta}d$ STATE

In this section we consider a possibility of a second superconducting transition in FeSe, caused by a transformation of the $s + d$ state into the $s + e^{i\eta}d$ state. Such an instability may arise near the point where the pairing interaction is attractive in both s -wave and d -wave channels, with comparable magnitudes. The parameter range of $s + e^{i\eta}d$ has been previously analyzed in Ref. [34], assuming that the nematic order is weak. Here we don't keep Φ small and include into consideration orbital transmutation in the nematic phase. We identify the parameter range, where $s + e^{i\eta}d$ order emerges.

To analyze the transition to $s + e^{i\eta}d$ -wave state, we numerically solve the full non-linear gap equations (B1-B3), including both s -wave and d -wave harmonics. We show our results in Fig. 15. In panel (a), we assume $J_{ee} = 0$ and vary the parameter α , which drives the system from

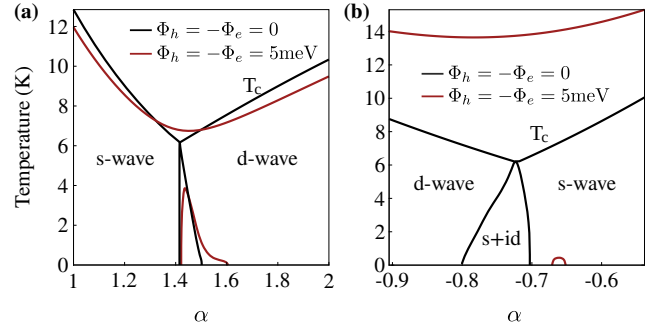


FIG. 15. Regions of the mixed $s + e^{i\eta}d$ order in the tetragonal and orthorhombic phases in the (T, α) plane. In (a) we set $J_{ee} = 0$ and $J_{eh} < 0$ to bring $\alpha = (U_{eh} - J_{eh})/(U_{eh} + J_{eh})$ close to $\sqrt{2}$. In (b) we set $J_{ee} = J_{eh} > 0$. A d -wave order develops when J_{eh}/U_{eh} is larger than a certain number. For our parameter, the mixed phase is located near $\alpha \sim -0.7$. The shrinking of the range of $s + e^{i\eta}d$ order with nematicity is stronger in (b) than in (a).

s - to d -wave symmetry at $\alpha \approx \sqrt{2}$. In panel (b) we set $J_{ee} = J_{eh}$, in this case the transition from s - to d -wave is at negative $\alpha \sim -0.7$. The black curves in the Fig. 15 are the results for $\Phi = 0$. In both panels, there is a sizable range of $s + id$ order, sandwiched between pure s -wave and d -wave states. This is consistent with Ref. [34]. For a finite nematic order, the gap function in the mixed state is $s + e^{i\eta}d$, where $0 \leq \eta \leq \frac{\pi}{2}$. The results for $\Phi \neq 0$ show that nematicity generally suppresses the width of the $s + e^{i\eta}d$ region, but the suppression is far stronger for $J_{ee} = J_{eh}$ (panel b) than for $J_{ee} = 0$ (panel a). The reason why a nematic order is unfavorable for the $s + e^{i\eta}d$ state is again orbital transmutation: as we said a nematic order makes pockets "mono-orbital" and therefore favors s -wave pairing. Consequently, the region, where s - and d -wave pairing channels are nearly degenerate, gets suppressed. We illustrate this in Fig. 16, where we plot the area of $s + e^{i\eta}d$ region, normalized to its value in the tetragonal state, and the difference in the orbital content on the hole pocket, both vs Φ_h . We see that the area of the mixed range shrinks and vanishes when Φ_h reaches Φ_{cr} .

Specific heat measurements on FeSe in Ref. [38–41] reported two jumps at $T_c = 8$ K and at $T^* \sim 1$ K. The jump at T_c clearly indicates the transition to the superconducting phase. In Ref. [34] it was argued that the jump at $T^* = 1$ K might be explained by the transition into the $s + e^{i\eta}d$ phase. Our results show that this is possible, but unlikely as the parameter range when $s + e^{i\eta}d$ order develops is quite narrow.

We also note in passing that in panel (b) of Fig. 15, T_c goes up at a nonzero Φ , despite that a nematic order is generally believed to be a competitor to superconductivity. This happens because J_{eh} is the dominant component of the pairing interaction, and J_{eh} couples d_{xz} fermions on the Γ -pocket to d_{yz} fermions on the X -pocket. The spectral weight of both fermions get en-

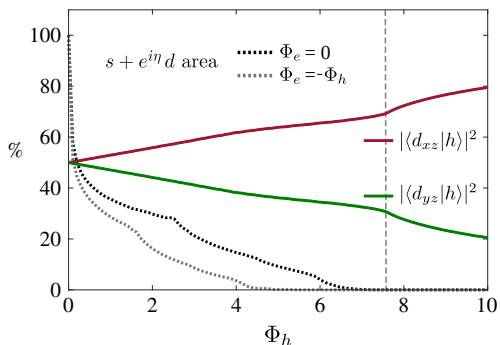


FIG. 16. The size of $s + e^{i\eta}d$ region (black) and the percentage of d_{xz} and d_{yz} orbital content at the hole pocket (red and green), vs Φ_h . Black-dashed line is for $\Phi_e = 0$, gray-dashed one is for $\Phi_e = -\Phi_h$.

hanced by sign-changing $d_{xz/yz}$ nematicity, and this enhances T_c . For the case in panel (a), the dominant interaction is U_{eh} that couples d_{xz} (d_{yz}) orbitals at Γ with d_{xz} (d_{yz}) orbitals at Y (X). In the nematic phase d_{xz} (d_{yz}) weight is enhanced (reduced) at Γ but reduced (enhanced) at Y (X). As a consequence, T_c is weakly affected by nematicity.

VI. CONCLUSIONS

In this paper we presented in-depth analysis of superconducting gap function and specific heat of a multi-orbital metal, like FeSe, which first develops a nematic order and then undergoes a transition into a superconducting state, which co-exists with nematicity. We considered two scenarios: scenario A, in which nematic order develops between d_{xz} and d_{yz} orbitals on hole and electron pockets (Φ_h and Φ_e) and scenario B, in which there is an additional component of the nematic order for d_{xy} fermions on the two electron pockets (Φ_{xy}).

We specifically addressed three questions. The first one is the angular dependence of the gap. Here we analyzed the competition between the two effects. One is nematicity-induced $s - d$ mixture, which necessary induces angular variation of the gap function even if the superconducting state is an s-wave without nematicity. Another one is orbital transmutation of low-energy excitations in the nematic state. This effect tends to make Fermi surface pockets mono-orbital and thus favors an angle-independent gap function. We analyzed the crossover from initial $s - d$ mixing to eventual angle-independent gap and argued that the most likely scenario for stronger s-wave attraction in the tetragonal phase is a gap function with no nodes, while for stronger d -wave attraction the 4 nodes from d -wave order disappear

once nematic order exceeds a certain threshold. However, in a parameter range where s-wave and d -wave interactions have comparable strength, we find more involved crossovers in which, e.g., the number of nodal points goes from zero to a finite number and then back to zero, or when the number of nodal points goes from 4 to 8 and then to zero.

The second question that we addressed is the behavior of a specific heat in a nematic superconductor. For this, we solved the non-linear gap equation, obtained the forms of the gaps below T_c , and used them to compute the specific heat $C_v(T)$. We analyzed the evolution of $C_v(T)$ with the nematic order in both the scenario A and the scenario B. Here our key result is the specific heat jump at T_c : $\Delta C_v/C_v$. We found that $\Delta C_v/C_v$ is around one in the tetragonal phase, for parameters appropriate for FeSe. The magnitude of $\Delta C_v/C_v$ increases with the nematic order and saturates at $\Delta C_v/C_v \sim 1.5 - 1.6$. This is quite consistent with the experimental result for FeSe $\Delta C_v/C_v \sim 1.65$ (Refs. [38–42, 46–50]). The values of $\Phi_{h,e}$ requires to reach saturation are smaller in scenario B as in this scenario the normal state $C_v(T)$ is smaller as it assumes that the Y pocket disappears because of sizable Φ_{xy} .

The third question that we addressed is a potential transition at $T_{c1} < T_c$ from an $s + d$ state to an $s + e^{i\eta}d$ state that breaks time-reversal symmetry. Such a transition was suggested [34] as a possible explanation of the experiments [38–42], which observed a second jump of $C_v(T)$ at $T^* \sim 1K$, well below $T_c \sim 8.5K$. At small $\Phi_{h,e}$, previous study found [34] that the parameter range where $s + e^{i\eta}d$ state develops at $T \rightarrow 0$ is quite sizable. We analyzed larger $\Phi_{h,e}$ and found that the range shrinks due to orbital transmutation which acts against competition between s- and d -pairing. We expect that the measurements of the gap function and specific heat in doped FeSe $_{1-x}$ S $_x$ or FeSe $_{1-x}$ Te $_x$, where the amount of nematic order varies with x , could verify the presence of the $s + e^{i\eta}d$ state.

VII. ACKNOWLEDGMENTS

We thank Rafael Fernandes, Thierry Klein, and Hai-Hu Wen for useful conversations. The work by KRI and AVC was supported by US Department of Energy, Office of Science, Basic Energy Sciences, under Award No. DE-SC0014402. The work of JB and IME was supported by the joint NSFC-DFG grant (ER 463/14-1)

* These two authors equally contributed to this work.

¹ Amalia I. Coldea and Matthew D. Watson, “The key ingredients of the electronic structure of fese,” Annual Review

- ² A. E. Böhmer and A. Kreisel, “Nematicity, magnetism and superconductivity in fese,” *J. Phys. Cond. Mat.* **30**, 023001 (2017).
- ³ Rafael M Fernandes and Andrey V Chubukov, “Low-energy microscopic models for iron-based superconductors: a review,” *Reports on Progress in Physics* **80**, 014503 (2016).
- ⁴ YS Kushnirenko, DV Evtushinsky, TK Kim, I Morozov, L Harnagea, S Wurmehl, S Aswartham, B Büchner, AV Chubukov, and SV Borisenko, “Nematic superconductivity in lifeas,” *Physical Review B* **102**, 184502 (2020).
- ⁵ Yuan Cao, Daniel Rodan-Legrain, Jeong Min Park, Noah F. Q. Yuan, Kenji Watanabe, Takashi Taniguchi, Rafael M. Fernandes, Liang Fu, and Pablo Jarillo-Herrero, “Nematicity and competing orders in superconducting magic-angle graphene,” *Science* **372**, 264–271 (2021).
- ⁶ K. Matano, M. Kriener, K. Segawa, Y. Ando, and Guoqing Zheng, “Spin-rotation symmetry breaking in the superconducting state of $\text{Cu}_x\text{Bi}_2\text{Se}_3$,” *Nature Physics* **12**, 852 (2016).
- ⁷ Shingo Yonezawa, Kengo Tajiri, Suguru Nakata, Yuki Nagai, Zhiwei Wang, Kouji Segawa, Yoichi Ando, and Yoshiteru Maeno, “Thermodynamic evidence for nematic superconductivity in $\text{Cu}_x\text{Bi}_2\text{Se}_3$,” *Nature Physics* **13**, 123 (2017).
- ⁸ Y. Pan, A. M. Nikitin, G. K. Araizi, Y. K. Huang, Y. Matsushita, T. Naka, and A. de Visser, “Rotational symmetry breaking in the topological superconductor $\text{Sr}_x\text{Bi}_2\text{Se}_3$ probed by upper-critical field experiments,” *Sci. Rep.* **6**, 28632 (2016).
- ⁹ Tomoya Asaba, B. J. Lawson, Colin Tinsman, Lu Chen, Paul Corbae, Gang Li, Y. Qiu, Y. S. Hor, Liang Fu, and Lu Li, “Rotational symmetry breaking in a trigonal superconductor nb-doped Bi_2Se_3 ,” *Phys. Rev. X* **7**, 011009 (2017).
- ¹⁰ Rafael M Fernandes and Oskar Vafek, “Distinguishing spin-orbit coupling and nematic order in the electronic spectrum of iron-based superconductors,” *Physical Review B* **90**, 214514 (2014).
- ¹¹ Luke C. Rhodes, Jakob Böker, Marvin A. Müller, Matthias Eschrig, and Ilya M. Eremin, “Non-local dxy nematicity and the missing electron pocket in fese,” *npj Quantum Materials* **6**, 45 (2021).
- ¹² M. D. Watson, T. K. Kim, A. A. Haghighirad, N. R. Davies, A. McCollam, A. Narayanan, S. F. Blake, Y. L. Chen, S. Ghannadzadeh, A. J. Schofield, M. Hoesch, C. Meingast, T. Wolf, and A. I. Coldea, “Emergence of the nematic electronic state in fese,” *Phys. Rev. B* **91**, 155106 (2015).
- ¹³ Andrey V Chubukov, Maxim Khodas, and Rafael M Fernandes, “Magnetism, superconductivity, and spontaneous orbital order in iron-based superconductors: Which comes first and why?” *Physical Review X* **6**, 041045 (2016).
- ¹⁴ Seiichiro Onari, Youichi Yamakawa, and Hiroshi Kontani, “Sign-reversing orbital polarization in the nematic phase of fese due to the c 2 symmetry breaking in the self-energy,” *Physical review letters* **116**, 227001 (2016).
- ¹⁵ Laura Fanfarillo, Joseph Mansart, Pierre Toulemonde, Hervé Cercellier, Patrick Le Fevre, François Bertran, Belen Valenzuela, Lara Benfatto, and Véronique Brouet, “Orbital-dependent fermi surface shrinking as a fingerprint of nematicity in fese,” *Physical Review B* **94**, 155138 (2016).
- ¹⁶ Lara Benfatto, Belén Valenzuela, and Laura Fanfarillo, “Nematic pairing from orbital-selective spin fluctuations in fese,” *npj Quantum Materials* **3**, 1–7 (2018).
- ¹⁷ Mattia Udina, Marco Grilli, Lara Benfatto, and Andrey V. Chubukov, “Raman response in the nematic phase of fese,” *Phys. Rev. Lett.* **124**, 197602 (2020).
- ¹⁸ Rui-Qi Xing, Laura Classen, Maxim Khodas, and Andrey V. Chubukov, “Competing instabilities, orbital ordering, and splitting of band degeneracies from a parquet renormalization group analysis of a four-pocket model for iron-based superconductors: Application to fese,” *Phys. Rev. B* **95**, 085108 (2017); Laura Classen, Rui-Qi Xing, Maxim Khodas, and Andrey V. Chubukov, “Interplay between magnetism, superconductivity, and orbital order in 5-pocket model for iron-based superconductors: Parquet renormalization group study,” *Phys. Rev. Lett.* **118**, 037001 (2017); S.H. Baek, D.V. Efremov, J. M. Ok, J. S. Kim, J van den Brink, and B. Büchner, “Orbital-driven nematicity in fese,” *Nature Materials* **14**, 210 (2014); Rui-Qi Xing, Laura Classen, and Andrey V. Chubukov, “Orbital order in fese: The case for vertex renormalization,” *Phys. Rev. B* **98**, 041108 (2018).
- ¹⁹ M. D. Watson, A. A. Haghighirad, L. C. Rhodes, M. Hoesch, and T. K. Kim, “Electronic anisotropies revealed by detwinned angle-resolved photo-emission spectroscopy measurements of FeSe,” *New J. Phys.* **19**, 103021 (2017).
- ²⁰ M. Yi, H. Pfau, Y. Zhang, Y. He, H. Wu, T. Chen, Z. R. Ye, M. Hashimoto, R. Yu, Q. Si, D.-H. Lee, Pengcheng Dai, Z.-X. Shen, D. H. Lu, and R. J. Birgeneau, “Nematic Energy Scale and the Missing Electron Pocket in FeSe,” *Phys. Rev. X* **9**, 041049 (2019).
- ²¹ S. S. Huh, J. J. Seo, B. S. Kim, S. H. Cho, J. K. Jung, S. Kim, Y. Y. Koh, C. I. Kwon, J. S. Kim, W. S. Kyung, J. D. Denlinger, Y. H. Kim, B. N. Chae, N. D. Kim, Y. K Kim, and C. Kim, “Absence of Y-pocket in 1-Fe Brillouin zone and reversed orbital occupation imbalance in FeSe,” *Commun. Phys.* **3**, 52 (2020).
- ²² C. Cai, T. T. Han, Z. G. Wang, L. Chen, Y. D. Wang, Z. M. Xin, M. W. Ma, Yuan Li, and Y. Zhang, “Momentum-resolved measurement of electronic nematic susceptibility in the $\text{FeSe}_{0.9}\text{S}_{0.1}$ superconductor,” *Phys. Rev. B* **101**, 180501 (2020).
- ²³ C. Cai, T. T. Han, Z. G. Wang, L. Chen, Y. D. Wang, Z. M. Xin, M. W. Ma, Yuan Li, and Y. Zhang, “Anomalous spectral weight transfer in the nematic state of iron-selenide superconductor,” *Chinese Physics B* (2020).
- ²⁴ L. C. Rhodes, M. D. Watson, A. A. Haghighirad, D. V. Evtushinsky, and T. K. Kim, “Revealing the single electron pocket of FeSe in a single orthorhombic domain,” *Phys. Rev. B* **101**, 235128 (2020).
- ²⁵ Daniel Steffensen, Andreas Kreisel, P. J. Hirschfeld, and Brian M. Andersen, “Interorbital nematicity and the origin of a single electron fermi pocket in fese,” *Phys. Rev. B* **103**, 054505 (2021).
- ²⁶ Nicola Lanata, Hugo UR Strand, Gianluca Giovannetti, Bo Hellsing, Luca de’Medici, and Massimo Capone, “Orbital selectivity in hund’s metals: The iron chalcogenides,” *Physical Review B* **87**, 045122 (2013).
- ²⁷ L. de’ Medici, *Weak and Strong Correlations in Fe Superconductors.*, Vol. 211 (Springer Series in Materials Science, United States, 2015).
- ²⁸ Andrey Chubukov, “Pairing mechanism in fe-based superconductors,” *Annual Review of Condensed Matter Physics* **3**, 57–92 (2012).

- ²⁹ P.J. Hirschfeld, “Using gap symmetry and structure to reveal the pairing mechanism in fe-based superconductors,” *Comptes Rendus Physique* **17**, 197 (2016).
- ³⁰ J. K. Glasbrenner, I. I. Mazin, Harald O. Jeschke, P. J. Hirschfeld, R. M. Fernandes, and Roser Valenti, “Effect of magnetic frustration on nematicity and superconductivity in iron chalcogenides,” *Nature Physics* **11**, 953 (2015).
- ³¹ Elena Bascones, Belén Valenzuela, and Maria José Calderón, “Magnetic interactions in iron superconductors: A review,” *Comptes Rendus Physique* **17**, 36 – 59 (2016).
- ³² S. Graser, T.A. Maier, P.J. Hirschfeld, and D.J. Scalapino, “Near-degeneracy of several pairing channels in multi-orbital models for the fe-pnictides,” *New J. Phys.* **11**, 025016 (2009).
- ³³ Jian Kang, Rafael M Fernandes, and Andrey Chubukov, “Superconductivity in fese: the role of nematic order,” *Physical review letters* **120**, 267001 (2018).
- ³⁴ Jian Kang, Andrey V Chubukov, and Rafael M Fernandes, “Time-reversal symmetry-breaking nematic superconductivity in fese,” *Physical Review B* **98**, 064508 (2018).
- ³⁵ P.O. Sprau, A Kostin, A Kreisel, A. E. Böhmer, Taoufour V., P. C. Canfield, S Mukherjee, P. J. Hirschfeld, B. M. Andersen, and J. C. Séamus Davis, “Discovery of orbital-selective cooper pairing in fese,” *Science* **357**, 75 (2017); Andreas Kreisel, Brian M. Andersen, P. O. Sprau, A. Kostin, J. C. Séamus Davis, and P. J. Hirschfeld, “Orbital selective pairing and gap structures of iron-based superconductors,” *Phys. Rev. B* **95**, 174504 (2017).
- ³⁶ Matthew D Watson, Amir A Haghighirad, Luke C Rhodes, Moritz Hoesch, and Timur K Kim, “Electronic anisotropies revealed by detwinned angle-resolved photoemission spectroscopy measurements of fese,” *New Journal of Physics* **19**, 103021 (2017); A. Fedorov, A. Yaresko, T. K. Kim, Y. Kushnirenko, E. Haubold, T. Wolf, M. Hoesch, A. Gruneis, B. Buechner, and S. V. Borisenko, “Effect of nematic ordering on electronic structure of fese,” *Scientific Reports* **6**, 36834 (2017).
- ³⁷ Dmitry V Chichinadze and Andrey V Chubukov, “Specific heat in strongly hole-doped iron-based superconductors,” *Physical Review B* **99**, 024509 (2019).
- ³⁸ Guan-Yu Chen, Xiyu Zhu, Huan Yang, and Hai-Hu Wen, “Highly anisotropic superconducting gaps and possible evidence of antiferromagnetic order in fese single crystals,” *Physical Review B* **96**, 064524 (2017).
- ³⁹ Yue Sun, Shunichiro Kittaka, Shota Nakamura, Toshiro Sakakibara, Koki Irie, Takuya Nomoto, Kazushige Machida, Jingting Chen, and Tsuyoshi Tamegai, “Gap structure of fese determined by angle-resolved specific heat measurements in applied rotating magnetic field,” *Physical Review B* **96**, 220505(R) (2017).
- ⁴⁰ Yue Sun, Shunichiro Kittaka, Shota Nakamura, Toshiro Sakakibara, Peng Zhang, Shik Shin, Koki Irie, Takuya Nomoto, Kazushige Machida, Jingting Chen, and Tsuyoshi Tamegai, “Disorder-sensitive nodelike small gap in fese,” *Phys. Rev. B* **98**, 064505 (2018).
- ⁴¹ Lin Jiao, Chien-Lung Huang, Sahana Rößler, Cevriye Koz, Ulrich K. Rößler, Ulrich Schwarz, and Steffen Wirth, “Superconducting gap structure of fese,” *Scientific Reports* **7**, 44024 (2017).
- ⁴² H. Cercellier, P. Rodière, P. Toulemonde, C. Marcenat, and T. Klein, “Influence of the quasiparticle spectral weight in fese on spectroscopic, magnetic, and thermodynamic properties,” *Phys. Rev. B* **100**, 104516 (2019).
- ⁴³ Thierry Klein et al., private communication.
- ⁴⁴ Vladimir Cvetkovic and Oskar Vafek, “Space group symmetry, spin-orbit coupling, and the low-energy effective hamiltonian for iron-based superconductors,” *Physical Review B* **88**, 134510 (2013).
- ⁴⁵ Morten H. Christensen, Rafael M. Fernandes, and Andrey V. Chubukov, “Orbital transmutation and the electronic spectrum of fese in the nematic phase,” *Phys. Rev. Research* **2**, 013015 (2020).
- ⁴⁶ J-Y Lin, YS Hsieh, DA Chareev, AN Vasiliev, Y Parsons, and HD Yang, “Coexistence of isotropic and extended s-wave order parameters in fese as revealed by low-temperature specific heat,” *Physical Review B* **84**, 220507 (2011).
- ⁴⁷ Frédéric Hardy, Mingquan He, Liran Wang, Thomas Wolf, Peter Schweiss, Michael Merz, Maik Barth, Peter Adelman, Robert Eder, Amir-Abbas Haghighirad, and Christoph Meingast, “Calorimetric evidence of nodal gaps in the nematic superconductor fese,” *Physical Review B* **99**, 035157 (2019).
- ⁴⁸ Y Mizukami, M Haze, O Tanaka, K Matsuura, D Sano, J Böker, I Eremin, S Kasahara, Y Matsuda, and T Shibauchi, “Non-local d_{xy} nematicity and the missing electron pocket in fese,” arXiv preprint arXiv:2105.00739 (2020).
- ⁴⁹ S Karlsson, P Strobel, A Sulpice, C Marcenat, M Legendre, F Gay, S Pairis, O Leynaud, and P Toulemonde, “Study of high-quality superconducting FeSe single crystals: crossover in electronic transport from a metallic to an activated regime above 350 k,” *Superconductor Science and Technology* **28**, 105009 (2015).
- ⁵⁰ Sahana Rößler, Chien-Lung Huang, Lin Jiao, Cevriye Koz, Ulrich Schwarz, and Steffen Wirth, “Influence of disorder on the signature of the pseudogap and multigap superconducting behavior in fese,” *Phys. Rev. B* **97**, 094503 (2018).
- ⁵¹ F. Marsiglio and J. P. Carbotte, “Strong-coupling corrections to bardeen-cooper-schrieffer ratios,” *Phys. Rev. B* **33**, 6141–6146 (1986).
- ⁵² J. P. Carbotte, “Properties of boson-exchange superconductors,” *Rev. Mod. Phys.* **62**, 1027–1157 (1990).
- ⁵³ T. M. Mishonov, S. I. Klenov, and E. S. Penev, “Temperature dependence of specific heat and penetration depth of anisotropic-gap bardeen-cooper-schrieffer superconductors for a factorizable pairing potential,” *Phys. Rev. B* **71**, 024520 (2005).
- ⁵⁴ Todor M. Mishonov, Valery L. Pokrovsky, and Hongduo Wei, “Thermodynamics of MgB_2 described by the weak-coupling two-band bcs model,” *Phys. Rev. B* **71**, 012514 (2005).
- ⁵⁵ E. J. Nicol and J. P. Carbotte, “Properties of the superconducting state in a two-band model,” *Phys. Rev. B* **71**, 054501 (2005).
- ⁵⁶ M. Zehetmayer, H. W. Weber, and E. Schachinger, “Separable model calculations for the anisotropic properties of mgb_2 ,” *Journal of Low Temperature Physics* **133**, 407–420 (2003).
- ⁵⁷ M Zehetmayer, “A review of two-band superconductivity: materials and effects on the thermodynamic and reversible mixed-state properties,” *Superconductor Science and Technology* **26**, 043001 (2013).
- ⁵⁸ Saurabh Maiti and Andrey V. Chubukov, “Renormalization group flow, competing phases, and the structure of superconducting gap in multiband models of iron-based superconductors,” *Phys. Rev. B* **82**, 214515 (2010).

Appendix A: Singularities in the hole coherence factor

In this section, we compute $\langle \cos 2\phi_h \rangle$ and $\langle \cos^2 2\phi_h \rangle$ as a function of Φ_h and show, respectively, that they exhibit an $x \ln|x|$ and $x^2 \ln|x|$ type non-analyticity near the critical nematic strength Φ_{cr} (defined below). Using Eqs.(5,7), we write $\cos 2\phi_h$ on the Fermi surface as,

$$\cos 2\phi_h = \frac{b \frac{\mathbf{k}_F(\theta)^2}{2} \cos(2\theta_h) - \Phi_h}{\frac{\mathbf{k}_F(\theta)^2}{2m_h} - \mu_h} \quad (\text{A1})$$

Here, $\mathbf{k}_F(\theta)$ is the Fermi radius at an angle θ . We define $\frac{\mathbf{k}_F^2}{2} = x_f(\theta)$ for convenience, and write

$$\begin{aligned} \cos 2\phi_h &= \frac{bx_f(\theta) \cos(2\theta_h) - \Phi_h}{\frac{x_f(\theta)}{m_h} - \mu_h} \\ &= m_h b \frac{bx_f(\theta) \cos(2\theta_h) - \Phi_h}{bx_f(\theta) - \Phi_{cr}}, \end{aligned} \quad (\text{A2})$$

where $\Phi_{cr} = \mu_h m_h b$ is the critical nematic strength where the orbital order in k_x -direction changes from d_{yz} to d_{xz} on the hole pocket. We set $m_h b = t$ for convenience and for our model parameters from TABLE-I, $t \approx 0.5$. We find the functional form of $bx_f(\theta)$ from the band dispersion Eq. (5) as,

$$bx_f(\theta) = \frac{\Phi_{cr} - t^2 \Phi_h \cos 2\theta + \sqrt{(\Phi_{cr} - t^2 \Phi_h \cos 2\theta)^2 - (1 - t^2)(\Phi_{cr}^2 - \Phi_h^2 t^2)}}{1 - t^2}. \quad (\text{A3})$$

In the limit where nematic order is small, i.e. $\Phi_h \ll \Phi_{cr}$ we can expand Eq. (A3) and Eq. (A2) in $\frac{\Phi_h}{\Phi_{cr}} \ll 1$, which yields

$$\langle \cos 2\phi_h \rangle_{FS} = -\frac{1-t}{2} \left(\frac{\Phi_h}{\Phi_{cr}} \right) - \frac{1-t^2}{16} \left(\frac{\Phi_h}{\Phi_{cr}} \right)^3 + O(\Phi_h^5), \quad (\text{A4})$$

$$\langle \cos^2 2\phi_h \rangle_{FS} = \frac{1}{2} - t \frac{1-t}{4} \left(\frac{\Phi_h}{\Phi_{cr}} \right)^2 + O(\Phi_h^4). \quad (\text{A5})$$

In the limit when $\Phi_h \approx \Phi_{cr}$, we find from Eq. (A3) precisely at $\Phi_h = \Phi_{cr}$

$$bx_f^{cr}(\theta, \Phi_{cr}) = \Phi_{cr} + \Phi_{cr} f(\theta), \quad (\text{A6})$$

where

$$f(\theta) = \frac{2t^2 \sin(\theta)^2 + 2t |\sin(\theta)| \sqrt{1 - t^2 \cos(\theta)^2}}{1 - t^2}. \quad (\text{A7})$$

Then,

$$\begin{aligned} \cos 2\phi_h &= t \frac{(\Phi_{cr} + \Phi_{cr} f(\theta)) \cos(2\theta) - \Phi_{cr}}{\Phi_{cr} + \Phi_{cr} f(\theta) - \Phi_{cr}} \\ &= t \left[-\frac{1}{f(\theta)} + \cos(2\theta) \left(1 + \frac{1}{f(\theta)} \right) \right] \\ &= t \left[\cos(2\theta) - 2 \frac{\sin(\theta)^2}{f(\theta)} \right]. \end{aligned} \quad (\text{A8})$$

From Eq. (A8), we find that near k_x -axis, $\cos 2\phi_h$ approaches the value t , while it is undefined in k_x -direction. We will show later $\cos 2\phi_h(0) = \text{sgn}(\Phi_{cr} - \Phi_h)$

$$\lim_{\theta \rightarrow 0} \cos 2\phi_h(\theta)_{\Phi_{cr}} = t. \quad (\text{A9})$$

Averaging $\cos 2\phi_h$ and $\cos^2 2\phi_h$ over the angle θ , we get,

$$\begin{aligned}\langle \cos 2\phi_h \rangle &= t \langle \cos(2\theta) \rangle - 2t \left\langle \frac{\sin(\theta)^2}{f(\theta)} \right\rangle \\ &= \frac{t}{2} - \frac{\sqrt{1-t^2}}{\pi} - \frac{\arcsin(t)}{\pi t} \\ &\approx -0.32,\end{aligned}\tag{A10}$$

$$\begin{aligned}\langle \cos^2 2\phi_h \rangle &= t^2 \left\langle \cos^2 2\theta + 4 \frac{\sin^4 \theta}{f(\theta)^2} - 4 \frac{\cos 2\theta \sin^2 \theta}{f(\theta)} \right\rangle \\ &= \frac{t(2(2-2t^2)\sqrt{1-t^2} + \pi t(2+t^2)) - 2 \arcsin t}{4\pi t^2} \\ &\approx 0.36.\end{aligned}\tag{A11}$$

Next we assume $\Phi_h = \Phi_{cr} + \delta$ and show how $\langle \cos 2\phi_h \rangle$ and $\langle \cos^2 2\phi_h \rangle$ depend on δ . Using Eq. (A3), we show,

$$bx_f(\theta, \delta) = \frac{\Phi_{cr} (1 - t^2 \cos(2\theta)) - \delta t^2 \cos(2\theta) + \sqrt{B}}{1 - t^2},\tag{A12}$$

where,

$$B = 4\Phi_{cr}^2 t^2 (1 - t^2 \cos(\theta)^2) \sin(\theta)^2 + \delta^2 t^2 - 4\delta^2 t^4 \sin(\theta)^2 \cos(\theta)^2 + 4\delta t^2 \Phi_{cr} \sin(\theta)^2 (1 - 2t^2 \cos(\theta)^2).\tag{A13}$$

At $\theta = 0, \pi$, $bx_f(0, \delta)$ has a $|\delta|$ type non-analyticity as we find from Eq. (A12)

$$bx_f(0, \delta) = \Phi_{cr} + \frac{t|\delta|}{1 + t \operatorname{sgn}(\delta)}\tag{A14}$$

and plot in Fig. 17. As a result, we find,

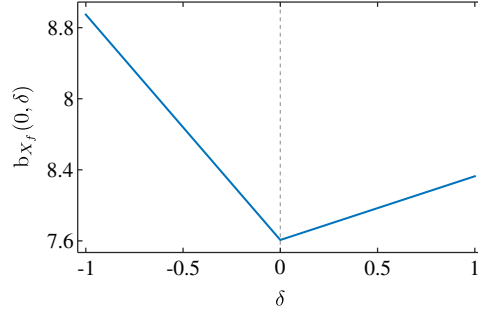


FIG. 17. $bx_f(0, \delta)$ as function of δ .

$$\begin{aligned}\cos 2\phi_h(0) &= t \frac{bx_f(0, \delta) - \Phi_{cr} - \delta}{bx_f(0, \delta) - \Phi_{cr}} \\ &= t \left(1 - \frac{\delta}{bx_f(0, \delta) - \Phi_{cr}} \right) \\ &= t \left(1 - \frac{\delta(1-t^2)}{|\delta|t - \delta t^2} \right) \\ &= -\operatorname{sgn}(\delta)\end{aligned}\tag{A15}$$

Next, we move to calculate $\langle \cos 2\phi_h \rangle$,

$$\begin{aligned}\langle \cos 2\phi_h \rangle &= t \left\langle \frac{bx_f(\theta, \delta) \cos(2\theta) - \Phi_h}{bx_f(\theta, \delta) - \Phi_{cr}} \right\rangle \\ &= t \left\langle \frac{bx_f(\theta, \delta) \cos(2\theta) - \Phi_{cr} - \delta}{bx_f(\theta, \delta) - \Phi_{cr}} \right\rangle \\ &= t \underbrace{\left\langle \frac{bx_f(\theta, \delta) \cos(2\theta) - \Phi_{cr}}{bx_f(\theta, \delta) - \Phi_{cr}} \right\rangle}_{\text{Term 1}} - \delta t \underbrace{\left\langle \frac{1}{bx_f(\theta, \delta) - \Phi_{cr}} \right\rangle}_{\text{Term 2}}.\end{aligned}\tag{A16}$$

We claim that the second blue under-braced term in Eq. (A16) contains the non-analytic behavior of $\langle \cos 2\phi_h \rangle$, because, as $\delta \rightarrow 0$, the denominator diverges at $\theta = 0$ and π , see Fig. 18(b). The first under-braced term in Eq. (A16) is almost independent of variations in δ , as can be seen in Fig. 18(a). Hence, we approximate the first term of

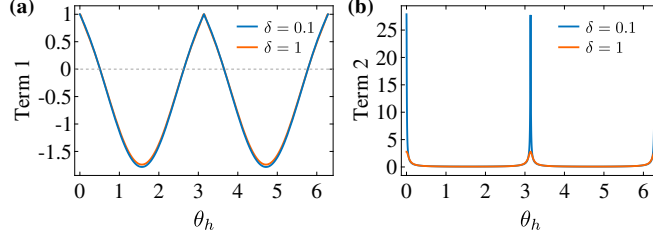


FIG. 18. We plot both of the integrands of Eq. A16 as a function of θ for $\delta = 0.1$ and 1.

Eq. (A16) by setting $\delta = 0$ and recover result of Eq. (A10).

To calculate the second term, we rewrite the denominator to separate the singular from the regular part,

$$\begin{aligned} bx_f(\theta, \delta) - \Phi_{cr} &= bx_f(\theta, \delta) - bx_f(0, \delta) + bx_f(0, \delta) - \Phi_{cr} \\ &= \frac{t|\delta|}{1 + t \operatorname{sgn}(\delta)} + (bx_f(\theta, \delta) - bx_f(0, \delta)). \end{aligned} \quad (\text{A17})$$

We again approximate that $(bx_f(\theta, \delta) - bx_f(0, \delta))$ does not change much with δ . So we write it as,

$$bx_f(\theta, \delta) - bx_f(0, \delta) \approx bx_f(\theta, 0) - bx_f(0, 0) = \phi_{cr} f(\theta). \quad (\text{A18})$$

Then, the non-analytic contribution of $\langle \cos 2\phi_h \rangle$ is,

$$\begin{aligned} \langle \cos 2\phi_h \rangle &= -\delta \left\langle \frac{1}{\Phi_{cr} f(\theta) + \frac{t|\delta|}{1+t \operatorname{sgn}(\delta)}} \right\rangle \\ &= -x \left\langle \frac{1}{f(\theta) + A(x)} \right\rangle, \end{aligned} \quad (\text{A19})$$

where, $x = \frac{\delta}{\Phi_{cr}}$, and

$$A(x) = t \frac{|x|}{1 + t \operatorname{sgn}(x)}. \quad (\text{A20})$$

We perform the integration over θ in Eq. A19, and obtain

$$\langle \cos 2\phi_h \rangle = -2x \left[\underbrace{\frac{\arccos(t)}{A(x) - 1}}_{\text{Term 1}} + \underbrace{\frac{2 - A(x)}{1 - A(x)} \frac{\sqrt{1 - t^2}}{\sqrt{(2 - A(x))^2 t^2 - A(x)^2}} \tanh^{-1} \left(\frac{\sqrt{(2 - A(x))^2 t^2 - A(x)^2}}{(2 - A(x))t} \right)}_{\text{Term 2}} \right]. \quad (\text{A21})$$

As $\delta \rightarrow 0$, the first term of Eq. (A21) inside the parenthesis approaches a finite value ($-\arccos(t)$), while the second term blows up because of the \tanh^{-1} function (see Fig. 19). We neglect the regular part, and expand the second term around $x = 0$ to find the nonanalytic component which is of $|x| \log(|x|)$ form.

$$\langle \cos 2\phi_h \rangle \propto -2x \left(2 + t \frac{|x|}{1 + t \operatorname{sgn}(x)} \right) \left(\frac{1}{2t} + \frac{|x|}{4(1 + t \operatorname{sgn}(x))} \right) (c - \log(|x|)) \propto |x| \log(|x|) \quad (\text{A22})$$

Next, we compute $\langle \cos^2 2\phi_h \rangle$ in the following way,

$$\begin{aligned} \langle \cos^2 2\phi_h \rangle &= t^2 \left\langle \frac{bx_f(\theta, \delta) \cos(2\theta) - \Phi_{cr}}{bx_f(\theta, \delta) - \Phi_{cr}} \right\rangle^2 \\ &= t^2 \left[\left\langle \frac{(bx_f(\theta, \delta) \cos(2\theta) - \Phi_{cr})^2}{(bx_f(\theta, \delta) - \Phi_{cr})^2} \right\rangle + \delta^2 \left\langle \frac{1}{(bx_f(\theta, \delta) - \Phi_{cr})^2} \right\rangle - 2\delta \left\langle \frac{(bx_f(\theta, \delta) \cos(2\theta) - \Phi_{cr})}{(bx_f(\theta, \delta) - \Phi_{cr})^2} \right\rangle \right] \end{aligned} \quad (\text{A23})$$

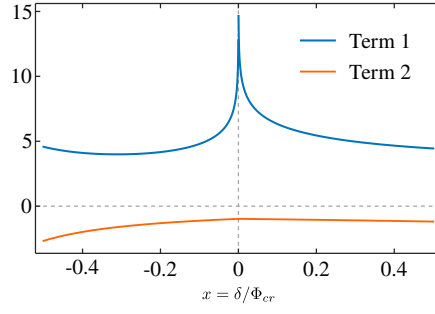


FIG. 19. Term 1 and Term 2 according to Eq. A21 as function of $x = \delta/\Phi_{cr}$

The first term of Eq. (A23) contains no singularity and gives the $\delta = 0$ contribution to $\langle \cos^2 2\phi_h \rangle$. To calculate the singularity present in the second term, we approximate the denominator as we did in Eq. (A17). We further approximate the function $f(\theta)$ near $\theta = 0$, where the non-analyticity is located and find

$$f(\theta) = \frac{2t}{\sqrt{1-t^2}} (\theta + A_2\theta^2 + O(\theta^3)), \quad (\text{A24})$$

where, $A_2 = \frac{t}{\sqrt{1-t^2}}$. Using Eq. (A24), we calculate the second term of Eq. (A23) as

$$t^2\delta^2 \left\langle \frac{1}{(bx_f(\theta, \delta) - \Phi_{cr})^2} \right\rangle = (1-t^2)x^2 \int_0^{\pi/2} \frac{1}{(\theta + A_2\theta^2 + A_0(x))^2}. \quad (\text{A25})$$

We define $A_0(x) = \frac{\sqrt{1-t^2}}{2}A(x)$. Eq. (A25) can be computed exactly, and is equal to,

$$x^2 \left(\frac{\pi}{A_0(x)(4A_0(x) + \pi(2 + A_2\pi))} - \frac{\pi(1 + A_2\pi)}{A_0(x)V(x)^2(4A_0(x) + \pi(2 + A_2\pi))} - 4\frac{A_2}{V(x)^3} \left[\arctan\left(\frac{1}{V(x)}\right) - \arctan\left(\frac{1 + A_2\pi}{V(x)}\right) \right] \right). \quad (\text{A26})$$

We define $V(x) = \sqrt{-1 + 4A_2A_0(x)}$. When $x \rightarrow 0$, $V(x) \rightarrow i$. The first and second term of Eq. (A26) are regular. To identify the non-analytic behaviour of the third term, we use the following identity Eq. (A27), and expand $V(x)$ up to the linear order in x ,

$$\arctan(z) = -\frac{i}{2} \log\left(\frac{1+iz}{1-iz}\right), \quad (\text{A27})$$

$$V(x) = i \left(1 - t^2 \frac{|x|}{1 + t \operatorname{sgn}(x)} \right) = i\tilde{V}(x), \quad (\text{A28})$$

where $\tilde{V}(x) = 1 - t^2 \frac{|x|}{1 + t \operatorname{sgn}(x)}$. Using Eq. (A27,A28), we find that,

$$\arctan\left(\frac{1}{V(x)}\right) = -\frac{i}{2} \log\left(\frac{\tilde{V}(x)+1}{\tilde{V}(x)-1}\right) \propto \log\left(\frac{t^2|x|}{1 + t \operatorname{sgn}(x)}\right). \quad (\text{A29})$$

Eq. (A29) shows that the most singular correction of Eq. (A26) is of the form $x^2 \log(|x|)$.

Finally, we write the last term of the Eq. (A23) in the following way to show that it is also singular of the form $x \log(x)$.

$$\begin{aligned} \delta \left\langle \frac{(bx_f(\theta, \delta) \cos(2\theta) - \Phi_{cr})}{(bx_f(\theta, \delta) - \Phi_{cr})^2} \right\rangle &= \delta \left\langle \frac{(bx_f(\theta, \delta) (1 - 2\sin^2\theta) - \Phi_{cr})}{(bx_f(\theta, \delta) - \Phi_{cr})^2} \right\rangle \\ &= \delta \left\langle \frac{1}{(bx_f(\theta, \delta) - \Phi_{cr})} \right\rangle - 2\delta \left\langle \frac{(bx_f(\theta, \delta) \sin^2\theta)}{(bx_f(\theta, \delta) - \Phi_{cr})^2} \right\rangle \end{aligned} \quad (\text{A30})$$

We show that the first term is singular of the form $x \log(|x|)$. We assume that the second term is not singular because of the $\sin^2 \theta$ term in the numerator.

Appendix B: BCS-gap equations

We treat Eq. (20) in mean field approximation and obtain the BCS-gap equations for the band-space gaps as

$$-\Delta_h(\mathbf{k}) = (U_s + U_d \cos 2\phi_h(\mathbf{k})) \int_{\mathbf{p}} \frac{\tanh \frac{E_X(\mathbf{p})}{2T}}{2E_X(\mathbf{p})} \cos^2 \phi_X(\mathbf{p}) \Delta_X(\mathbf{p}) \\ + (U_s - U_d \cos 2\phi_h(\mathbf{k})) \int_{\mathbf{p}} \frac{\tanh \frac{E_Y(\mathbf{p})}{2T}}{2E_Y(\mathbf{p})} \cos^2 \phi_Y(\mathbf{p}) \Delta_Y(\mathbf{p}) \quad (\text{B1})$$

$$-\Delta_X(\mathbf{k}) = \cos^2 \phi_X(\mathbf{k}) \left[\int_{\mathbf{p}} \frac{\tanh \frac{E_h(\mathbf{p})}{2T}}{2E_h(\mathbf{p})} (U_s + U_d \cos 2\phi_h(\mathbf{p})) \Delta_h(\mathbf{p}) + J_{ee} \int_{\mathbf{p}} \frac{\tanh \frac{E_Y(\mathbf{p})}{2T}}{2E_Y(\mathbf{p})} \cos^2 \phi_Y(\mathbf{p}) \Delta_Y(\mathbf{p}) \right] \quad (\text{B2})$$

$$-\Delta_Y(\mathbf{k}) = \cos^2 \phi_Y(\mathbf{k}) \left[\int_{\mathbf{p}} \frac{\tanh \frac{E_h(\mathbf{p})}{2T}}{2E_h(\mathbf{p})} (U_s - U_d \cos 2\phi_h(\mathbf{p})) \Delta_h(\mathbf{p}) + J_{ee} \int_{\mathbf{p}} \frac{\tanh \frac{E_X(\mathbf{p})}{2T}}{2E_X(\mathbf{p})} \cos^2 \phi_X(\mathbf{p}) \Delta_X(\mathbf{p}) \right], \quad (\text{B3})$$

where $E_i(\mathbf{p}) = (\xi_i^2(\mathbf{p}) + |\Delta_i(\mathbf{p})|^2)^{1/2}$ is the typical Bogoliubov quasiparticle spectrum and momentum integration is confined to an energy interval $[-\Lambda, \Lambda]$ around the Fermi surface. Near T_c the linearized gap equations are

$$\Delta_1 + \Delta_2 \cos 2\phi_h = -\log \frac{\Lambda}{T_c} \left[N_X \Delta_3 (U_s + U_d \cos 2\phi_h) \langle \cos^4 \phi_X \rangle + N_Y \Delta_4 (U_s - U_d \cos 2\phi_h) \langle \cos^4 \phi_Y \rangle \right] \quad (\text{B4})$$

$$\Delta_3 = -\log \frac{\Lambda}{T_c} \left[N_h \langle (U_s + U_d \cos 2\phi_h) (\Delta_1 + \Delta_2 \cos 2\phi_h) \rangle + N_Y \Delta_4 J_{ee} \langle \cos^4 \phi_Y \rangle \right] \quad (\text{B5})$$

$$\Delta_4 = -\log \frac{\Lambda}{T_c} \left[N_h \langle (U_s - U_d \cos 2\phi_h) (\Delta_1 + \Delta_2 \cos 2\phi_h) \rangle + N_X \Delta_3 J_{ee} \langle \cos^4 \phi_X \rangle \right] \quad (\text{B6})$$

Appendix C: Dependence of $\frac{\Delta_2}{\Delta_1}$ on the nematic order

We set $J_{ee} = 0$ in this section, and compute the ratio $\frac{\Delta_2}{\Delta_1}$ analytically. The largest eigenvalue λ of the matrix equation(24) corresponding to the leading superconducting instability turns out to be,

$$\lambda = \left[\frac{N_h}{2} \left[g_0 + 2\alpha \langle \cos 2\phi_h \rangle g_1 + \alpha^2 \langle \cos^2 2\phi_h \rangle g_0 + \right. \right. \\ \left. \left. + \sqrt{4\alpha^2 (\langle \cos 2\phi_h \rangle^2 - \langle \cos^2 2\phi_h \rangle) (g_0^2 - g_1^2) + (g_0 + 2\alpha \langle \cos 2\phi_h \rangle g_1 + \alpha^2 \langle \cos^2 2\phi_h \rangle g_0)^2} \right] \right]^{1/2}, \quad (\text{C1})$$

where

$$g_0 = N_X \langle \cos^4 \phi_X \rangle + N_Y \langle \cos^4 \phi_Y \rangle \quad (\text{C2})$$

and

$$g_1 = N_X \langle \cos^4 \phi_X \rangle - N_Y \langle \cos^4 \phi_Y \rangle \quad (\text{C3})$$

In the tetragonal phase, $g_1 = 0$ and $g_0 = 2N_X \langle \cos^4 \phi_X \rangle$ (for our band parameters, $g_0 \approx 0.1$). With increasing electron nematic order Φ_e , $\langle \cos^4 \phi_Y \rangle$ decreases since Y-pocket becomes mostly of d_{xy} nature. As a result, $g_0 - g_1$ decreases with Φ_e .

To calculate the ratio $\frac{\Delta_2}{\Delta_1}$, we rewrite Eq. (B4),

$$\Delta_2 = -\frac{\alpha}{\lambda} \left[N_X \Delta_3 \langle \cos^4 \phi_X \rangle - N_Y \Delta_4 \langle \cos^4 \phi_Y \rangle \right] \quad (\text{C4})$$

of Eq. (C4) can be computed from Eqs.(B5,B6), and we get the following relation,

$$\Delta_2 = \frac{N_h \alpha}{\lambda^2} [\Delta_1 (g_1 + \alpha \langle \cos 2\phi_h \rangle g_0) + \Delta_2 (g_1 \langle \cos 2\phi_h \rangle + \alpha \langle \cos^2 2\phi_h \rangle g_0)] \quad (\text{C5})$$

One rearranges Eq. (C5) to find the ratio,

$$\begin{aligned} \frac{\Delta_2}{\Delta_1} &= \alpha N_h \frac{g_1 + \alpha \langle \cos 2\phi_h \rangle g_0}{\lambda^2 - \alpha N_h (g_1 \langle \cos 2\phi_h \rangle + \alpha \langle \cos^2 2\phi_h \rangle g_0)} \\ &= 2\alpha \frac{g + \alpha \langle \cos 2\phi_h \rangle}{(1 - \alpha^2 \langle \cos^2 2\phi_h \rangle) + D}, \end{aligned} \quad (\text{C6})$$

where

$$D = \sqrt{4\alpha^2 (\langle \cos 2\phi_h \rangle^2 - \langle \cos^2 2\phi_h \rangle) (1 - g^2) + (1 + 2\alpha \langle \cos 2\phi_h \rangle g + \alpha^2 \langle \cos^2 2\phi_h \rangle)^2}, \quad (\text{C7})$$

and

$$g(\Phi_e) = \frac{g_1}{g_0} = \frac{N_X \langle \cos^4 \phi_X \rangle - N_Y \langle \cos^4 \phi_Y \rangle}{N_X \langle \cos^4 \phi_X \rangle - N_Y \langle \cos^4 \phi_Y \rangle}. \quad (\text{C8})$$

Even though nematic order couples *s*- and *d*-wave symmetry and brings angular dependence to the superconducting gap function in the primary *s*-wave state, one finds that $\frac{\Delta_2}{\Delta_1} = 0$ when the numerator of Eq. (C6) vanishes,

$$(N_X \langle \cos^4 \phi_X \rangle - N_Y \langle \cos^4 \phi_Y \rangle) + \alpha \langle \cos 2\phi_h \rangle (N_X \langle \cos^4 \phi_X \rangle + N_Y \langle \cos^4 \phi_Y \rangle) = 0. \quad (\text{C9})$$

For this case, the gap function on the hole pocket becomes purely *s*-wave, despite the presence of nematic order.
